EVALUATION OF METABOLIC ACTIVITY DIFFUSION IMAGING IN RESECTED HUMAN GLIOMAS

by

Jackson E. Herb

A THESIS

Presented to the Medical Physics Graduate Program
and the Oregon Health & Science University
School of Medicine
in partial fulfillment of
the requirements for the degree of

Master of Science

May 2025

Contents

Table of Contents iii

List of Abbreviations v

List of Tables vi

List of Figures viii

Acknowledgments xi

Abstract xii

1 Introduction 1
- 1.1 Biochemistry of MADI . . . 1
  - 1.1.1 Transcytolemmal Water Transport . . . 1
  - 1.1.2 Na^+,K^+-ATPase Ion Pump . . . 2
  - 1.1.3 MADI . . . 3
- 1.2 Glioma and Pseudoprogression . . . 4
  - 1.2.1 Warburg Effect . . . 4
  - 1.2.2 The Problem of Pseudoprogression . . . 5
- 1.3 Magnetic Resonance Imaging . . . 6
  - 1.3.1 T_1-weighted and T_2-weighted Imaging . . . 8
  - 1.3.2 Diffusion Weighted Imaging . . . 8
- 1.4 Positron Emission Tomography . . . 9
- 1.5 Motivations for MADI . . . 11
- 1.6 Project Goals . . . 12

2 Methods 13
- 2.1 Population . . . 13
- 2.2 Image Acquisitions . . . 14
- 2.3 MADI Map Creation . . . 15
- 2.4 Image Registration . . . 20
- 2.5 Image Analysis . . . 20
  - 2.5.1 Regions of Interest . . . 20

2.5.2 Data Collection 21
2.5.3 Data Processing 22
2.5.4 Kullback-Leibler Divergence 23
2.6 PET 25
2.7 Water Glucose Index 25

3 Results 27
3.1 Control Data 27
3.1.1 Grey and White Matter 27
3.1.2 $p(x)$ Consistency 29
3.2 MADI 31
3.2.1 pROI Selection 31
3.2.2 Tumor & Pseudoprogression & Half-Brain 31
3.3 PET 35
3.4 WGI 36

4 Discussions 38
4.1 Grey and White Matter - Reference and Scale 38
4.2 MADI 39
4.2.1 HBCL Control 39
4.2.2 pROI Selection 39
4.2.3 pROI to HBCL 40
4.3 PET 41
4.4 Considerations of Previous Works 41
4.5 Clinical Implementation 42
4.6 Limitations 43
4.6.1 MADI Library 43
4.6.2 Ill-Fitting Pixels 45
4.6.3 Sample Size 45
4.7 Future Work 46

5 Conclusions 48

Bibliography 49

A Appendix 55

List of Abbreviations

^{18}F-FDG: ^{18}F Fluorodeoxyglucose

ATP: Adenosine Triphosphate

^{c}MR$_{\text{AWC}}$: Cellular Metabolic Rate of active water cycling

^{c}MR$_{\text{glc}}$: Cellular Metabolic Rate of glucose

^{c}MR$_{\text{NKA}}$: Cellular Metabolic Rate of the Sodium Potassium ATPase Pump

DWI: Diffusion Weighted Imaging

FOV: Feild of View

Gd: Gadolinium

GM: Grey Matter

HBCL: Half-Brain Contralateral

IRB: Institutional Review Board

KDE: Kernel Density Estimation

KL: Kullback-Leibler

MA: Metabolic Activity

MADI: Metabolic Activity Diffusion Imaging

MRI: Magnetic Resonance Imager

NKA: Sodium Potassium ATPase Pump

NMR: Nuclear Magnetic Resonance

OHSU: Oregon Health & Science University

PDF: Probability Density Function

PET: Positron Emission Tomography

PMT: Photomultiplier Tube

pROI: Primary Region of Interest

RANO: Response Assessment in Neuro-Oncology RE: Relative Entropy

RF: Radiofrequency

ROI: Region of Interest

SE: Standard Error

SUV: Standard Uptake Value

T1post: T_1-weighted post-Gadolinium contrast

T1pre: T_1-weighted pre-Gadolinium contrast

T_{1w}: T_1-weighted

T_{2w}: T_2-weighted

TE: Echo time

$^{t}\mathrm{MR}_{\mathrm{glc}}$: Tissue Metabolic Rate of glucose

TR: Repetition Time

WGI: Water Glucose Index

WM: White Matter

List of Tables

2.1 Collection of participants' tumor type and designation of tumor or pseudoprogression. 14
2.2 Characterization of parameter grids use for normalization and KL divergence calculations. 24

A.1 Collection of average medians for each MADI parameter for tumor and pseudoprogression groups and in different locations in the brain. . . . 59

List of Figures

1.1 Water transport process associated with the NKA pump and cotransporters (active transport), and aquaporins (passive transport). 2

2.1 A single slice of a spin echo DWI image of participant 1388. Image contains b values 50, 360, 670, 980, 1290, 1600, 1910, 2220, 2530, 2840, 3150, 3460, 3770, 4080, 4390, and 4700 s/mm^2. 14

2.2 (Top) Slices of a T1post image of participant 1388. (Bottom) Individual slice from participant 1388's T1post image. 16

2.3 (Top) Slices of a ^{18}F-FDG-PET image of participant 1388. (Bottom) Individual slice from participant 1388's ^{18}F-FDG-PET image. 17

2.4 A Slice of maps of all MADI parameters of participant 1388: a) k_{io} [1/s], b) $k_{io}V$ [pL/s/cell], c) $k_{io}V\rho$ [10^5 pL/s/μL], d) ρ [10^5 cells/μL], e) V [pL/cell], and f) v_i [1]. pROI-Hollow is outlined in red. Images depicted underwent 20 pL/cell filtering. 19

2.5 Participant 1388's T1post image with pROI regions depicted. 21

2.6 Plots of ADC vs V on linear (left) and logrithmic (right) scales demonstrating scope of ill-fitting pixels. Orange and red line corresponds to 10 and 20 pL, respectively. Bifunctional behavior of data shown; exponential-like and linear-like. Data is reflective of participant 1950. 22

3.1 Comparison of GM and WM distributions from modified Figure 5 of Springer et al [1] (top) and each participant's contralateral (bottom). 28

3.2 Comparison of a T1pre (left) and V (right) image for visual differentiation of GM and WM. 29

3.3 The average RE of per participant WM to GM distributions. 30

3.4 The average RE of per participant half-brain contralateral PDF to the population's average PDF. 30

3.5 Comparison of per participant half-brain contralateral PDF to population averaged PDF. ρ (left) is the lowest RE parameter while $k_{io}V$ (right) is the highest. 31

3.6 Comparison of per participant GM contralateral PDF to population averaged PDF. 32

3.7 The grouped population's average RE of pROI to HBCL. Tumor group (left), pseudoprogression group (right). 32

3.8 The grouped population's average RE of pROI-Entire to half-brain contralateral. 33

3.9 The RE of the averaged pseudoprogression PDFs to the averaged tumor PDFs for pROI-Entire. 34

3.10 Plots of group averaged PDFs for $k_{io}V$ (left) and k_{io} (right) to represent the weakest and strongest cases for tumor-pseudoprogression-halfbrain differentiation. Vertical dashed lines represent each PDF's median value. 34

3.11 Plots of averaged medians with SE for all MADI parameters. 35

3.12 The relative enhancement ($\mathrm{SUV}^{\mathrm{pROI}}_{\mathrm{mean}}/\mathrm{SUV}^{\mathrm{comparison}}_{\mathrm{mean}}$) occurring within each participant's PET image. 36

3.13 Comparison of pROI-Entire's WGI to GM and WM. 37

4.1 Histograms of v_i within the Entire pROI for all participants. 44

4.2 Plot of ADC vs. V for pegged (red) and non-pegged (blue) v_i pixels. Data is reflective of participant 1950. 46

A.1 Plots of ADC vs V for all participants. Orange and red lines are 10 and 20 pL/cell, respective. Plots correspond to participants 1388 (top left), 1803 (top right), 1820 (bottom left), and 1950 (bottom right). . 56

A.2 Plots of ADC vs $\ln(V)$ for all participants. Orange and red lines are 10 and 20 pL/cell, respective. Plots correspond to participants 1388 (top left), 1803 (top right), 1820 (bottom left), and 1950 (bottom right). 57

A.3 Plots of ADC vs V in both linear and logarithmic scales for mice BIP-1 and BIP-4 used in Schlegel [2]. Orange and red lines are 10 and 20 pL/cell, respective. 58

A.4 Maps of $k_{io}V$ for all participants with pROI-Hollow. 60

Acknowledgments

For all the help and guidance throughout this project, I would like to thank my research advisor Dr. Pike. You have been amazingly kind and patient to me during the time we have worked together.

For their insight and support in creation of this Thesis, I would like to thank my committee members Dr. Cory Wyatt and Dr. Anna Mench.

A great amount of appreciation and thanks goes out to OHSU's Advanced Imaging Research Center faculty Eric Baker, Dr. Xin Li, and Dr. Charles Springer for all their contributions and assistance.

I would like to give thanks to my graduate program faculty, specifically, Dr. Lindsay DeWeese, Dr. Lindsay Douglas, Isaac Bailey, Dr. Celeste Winters, Dr. Anna Mench, and Dr. Cory Wyatt for providing me with ample opportunities to learn and develop skills. I feel confident and prepared going into my future career.

To my friends Kyle Markey and Kendall Shadduck, thank you for always being around and giving me plenty of opportunities to get away from school and enjoy my time off.

To my mom and dad, thank you for all the support. These last two years would've been significantly more difficult without you around!

Finally, to my wife Hannah, your love and unwavering belief carried me through this journey's hardest moments. No words can fully express my gratitude for your sacrifices and endless support. I love you. Thank you.

Abstract

The current state of clinical metabolic activity (MA) imaging is limited. With the few available options, such as positron emission tomography (PET) and hyperpolarized ^{13}C magnetic resonance imaging, requiring intravenous radioactive or hyperpolarized tracers and having relatively poor spatial resolution, there exists opportunities for advancement in the field. Oregon Health & Science University's Advanced Imaging Research Center has developed a novel non-invasive, contrast-agent-free, MRI-based metabolic activity diffusion imaging (MADI) approach providing multiple quantitative parameters and improved resolution over other clinical MA imaging methods. MADI is rooted in the trans-cytolemmal water exchange, where large contributions of exchange are stimulated by MA. This exchange is quantified as the homeostatic (steady-state) cellular H_2O efflux rate constant (k_{io}). By matching voxels of diffusion weighted imaging (DWI) b-space decays to a library of simulated decays within k_{io}, cellular density (ρ), and cellular volume (V) parameter-space, MADI is able to extract voxel cellular information and produce parameter maps. Products such as $k_{io} * V$ and $k_{io} * V * \rho$ can be made to probe MA as $k_{io}V$ is roughly proportional to activity of the $^{+}$Na/$^{+}$K ATPase, the major energy consumer in the cell. Representing the first study to employ the MADI approach in human brain cancer, four resected glioma participants with different tumor progression status were investigated: two tumor progression and two pseudoprogression. Regions of interest (ROI) were cre-

ated on T1-weighted pre- and post-gadolinium (Gd) contrast images registered to DWI images and applied to images of DWI and PET, also registered. The ROI of tumor or pseudoprogression were defined by the T1-weighted post-gadolinium contrast enhancement(s). Probability density functions (PDFs) and Kullback-Leibler (KL) divergence were used to characterize and analyze MADI parameter distributions. KL divergence requires consistency of comparison PDFs. The half-brain contralateral (HBCL) control data was deemed to satisfy this condition with maximum relative entropy (RE), the output of KL divergence, of 0.0160 ± 0.0076 nat and after visual inspection of PDFs. The data suggests that $k_{io}V$ was able to differentiate normal tissue, tumor, and pseudoprogression; RE of tumor and pseudoprogression to HBCL was 0.293 ± 0.093 and 0.891 ± 0.088 nat, respectively. As a more rudimentary but accessible representation, the average of $k_{io}V$ medians for HBCL, tumor, and pseudoprogression were 19.14 ± 0.49, 33.33 ± 4.24, and 54.21 ± 1.12 pL/s/cell, respectively. Despite having local enhancement of the tumor and pseudoprogression regions, PET was unable to differentiate tumor progression status in comparison to grey matter. Although a larger subject population is require to confirm the ability of MADI to distinguish these tissue states, this preliminary data show promise in MADI's ability to probe cellular properties and may provide great value for disease diagnosis and monitoring.

Chapter 1

Introduction

1.1 Biochemistry of MADI

1.1.1 Transcytolemmal Water Transport

Transcytolemmal water transport refers to how water is transported and exchanged across a cell membrane. Water transport can occur through multiple pathways and are categorized as either active or passive depending on the energy of the process. Passive water transport pathways do not require an input of energy and primarily occur due to osmosis, i.e. moving with its concentration gradient [3,4]. As an example, Aquaporin-4 performs crucial roles in regulating ion and volume homeostasis within the brain [5]. Active transport has further primary and secondary categorization depending on the mechanism of energy input. Transport mechanisms which use chemical energy, such as from ATP, to transport molecules to overcome their concentration gradient designates a primary active water transport. As of yet there are no known primary active water transport mechanisms. However, numerous cotranporters have been identified which are driven by the Na^+ or K^+ concentration gradients created by Sodium-Potassium ATPase (NKA) which are now known to also transport very large

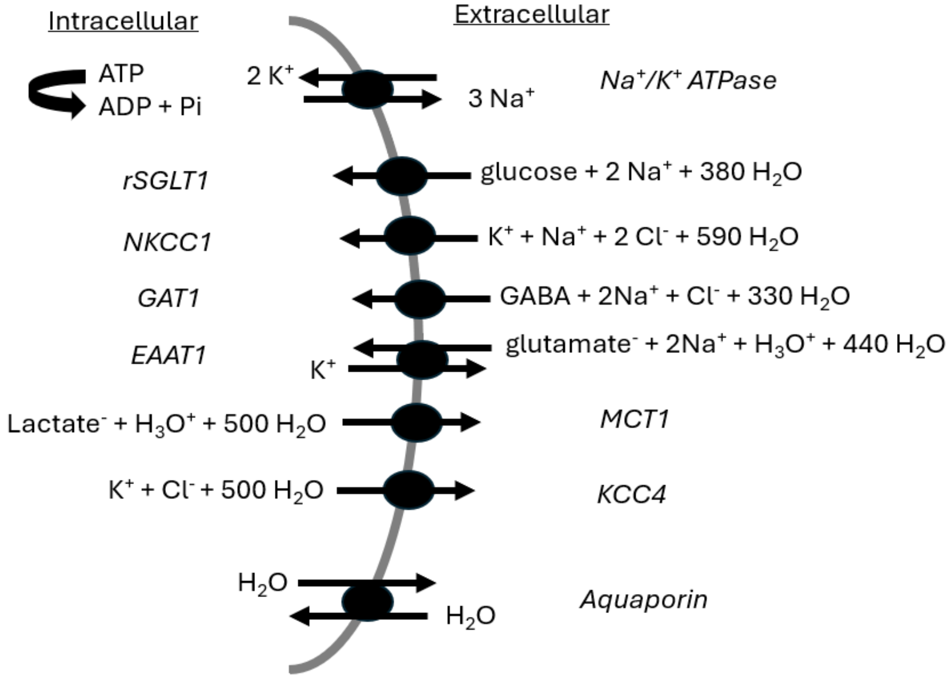

Figure 1.1 Water transport process associated with the NKA pump and cotransporters (active transport), and aquaporins (passive transport).

stoichiometries of water [4]. These include for example, as seen in Figure 1.1, the rSGLT1 contransporter which tranports glucose, $2Na^+$, and 380 H_2O into the cell, and the KCC4 cotransporter which transports K^+, Cl^-, and 500 H_2O out of the cell. As these are functionally coupled to NKA activity, they constitute secondary active water transport. This active transport of water is thought to constitute a large fraction of transcytolemmal water transport hence linking active water transport to NKA , the major energy consumer in the brain [6–8].

1.1.2 Na^+,K^+-ATPase Ion Pump

The NKA pump exchanges 3 sodium ions out of the cell and 2 potassium ions into the cell. As the extracellular concentration of sodium is greater than the intracellular, and the intracellular concentration of potassium is greater than the extracellular concentration, this process necessitates an energy input and is thus an energy dependent pump. Furthermore, this process moves a net positive charge out of the cell and against the membrane's electrochemical gradient, which also increases the energy input [6,9]. To generate this energy, the NKA pump performs ATP hydrolysis to produce ADP. This step is foundational to cellular metabolic activity (MA), thus NKA pump activity is directly related to MA [10]. This has been demonstrated in rats where fasted (glucose-lowered) neurons had a significant reduction in ATP levels and NKA pump activity than non-fasted neurons [11]. For most cells, the NKA pump bears a large proportion of the consumption of metabolic energy; for brain tissue it is estimated to be 55% [12].

1.1.3 MADI

Metabolic activity diffusion imaging (MADI) uses diffusion weighted imaging (DWI), to characterize cellular water diffusion and tissue composition via four parameters: k_{io} [units: 1/s], ρ [units: 10^5 cells/uL], V [units: pL/cell], and v_i [units: 1]. k_{io} is the homeostatic (steady-state) cellular water efflux (unidirectional) rate constant, but can also be interpreted as the inverse of the mean lifetime of water within a cell. k_{io} quantifies transmembrane water cycling, which is linked to NKA activity and cellular energy use, making it a crucial metabolic indicator [13, 14]. ρ and V are cellular density and cellular volume within a voxel, respectively. Lastly, v_i is the fractional cellular volume describing how much of a voxel is being occupied by cells and is related to volume and density by $v_i = \rho V$. By taking voxel-wise products of MADI parameters we can convert the k_{io} rate constant to rates of water efflux per cell ($k_{io}V$, units: [pL/s/cell]) and per tissue volume ($k_{io}V\rho$, units: [pL/s/uL]). A significant portion of water efflux is linked to NKA activity allowing these rates to estimate in vivo homeostatic NKA metabolic rate (${}^c\mathrm{MR}_{\mathrm{NKA}}$), which has not been previously quantified in vivo. Since active transcellular water flux, proportional to ${}^{c}\mathrm{MR}_{\mathrm{NKA}}$, is a large part of total transcellular water flux, $k_{io}V$ indirectly measures ${}^{c}\mathrm{MR}_{\mathrm{NKA}}$. Currently, $k_{io}V$ is the sole non-invasive indicator of NKA activity, representing a novel metabolic activity biomarker [1, 6–8, 15].

1.2 Glioma and Pseudoprogression

Glioma is an umbrella term for a primary type of brain tumor which occurs in the glial cells of the brain or spinal cord and has various classifications and gradings. For low-grade tumors, such as oligodendroglioma, a patient's median survival may be anywhere between 11.6 to 16.7 years, but unfortunately within 5 to 10 years 70% of cases progress to high-grade tumors [16–18]. High-grade tumors, such as glioblastoma, are some of the most aggressive with a median overall survival of approximately 3 years. Glioblastoma's incident rate is 3.19 per 100,000 persons within the United States with a median age of diagnosis of 64 years [19].

1.2.1 Warburg Effect

In healthy differentiated tissue with ample oxygen supply, cellular metabolism is driven by oxidative phosphorylation. This process is incredibly efficient producing roughly 36 ATP molecules per glucose molecule. If the tissue is deficient in oxygen supply, it will instead metabolize glucose using anaerobic glycolysis. This process only nets roughly 2 ATP per glucose. In tumorous tissue, metabolism of glucose by oxidative phosphorylation still occurs, but at reduced rates. Instead, a shift occurs causing glucose to be metabolized by aerobic glycolysis at significantly higher rates. This process is also inefficient at roughly 4 ATP per glucose. This inefficient process is thought to be at the benefit of tumors as it allows for increased cancerous biomass synthesis, has a quicker ATP production, and leads to microenvironment conditions suitable for tumor cells [20–23]. This cellular reprogramming of metabolism is what characterizes the Warburg Effect; the alteration of ATP production from energy metabolites in tumor cells.

1.2.2 The Problem of Pseudoprogression

The diagnosis of cancers, including gliomas, is continually evolving with advances in understanding and technology. The Response Assessment in Neuro-Oncology (RANO) working group has established criteria for glioma response assessment using magnetic resonance imaging (MRI) and amino acid positron emission tomography (PET). A significant challenge, particularly post-surgically and following treatments like radiation and chemotherapy, is differentiating true tumor progression from pseudoprogression. Pseudoprogression, characterized by increased contrast enhancement on MRI, mimics tumor progression but represents vascular changes and treatment-related inflammation, potentially leading to misdiagnosis and inappropriate treatment [24, 25]. This highlights the need for advanced imaging and integrated diagnostic approaches.

Recent research has focused on the role of ^{18}F fluorodeoxyglucose PET (^{18}F-FDG-PET) in glioma assessment alongside MRI, especially gadolinium-contrast (Gd) MRI and diffusion-weighted imaging (DWI). While amino acid PET tracers are increasingly used, ^{18}F-FDG-PET remains widely available, offering complementary information to MRI. Studies indicate that combined ^{18}F-FDG-PET and MRI has improved prognostic prediction, recurrence detection, and aids in treatment planning and response evaluation [26–28].

1.3 Magnetic Resonance Imaging

MRI is an imaging method, with origins in nuclear magnetic resonance (NMR) spectroscopy, where interactions between nuclear spins and magnetic fields are manipulated and measured to create signals that are then reconstructed into images. In general MRI methods, the nuclear spins being probed are the proton from hydrogen nuclei of water, i.e. ^{1}H MRI. In the absence of an external magnetic field, proton spins are randomly oriented. When an external field (B_0) is applied, protons can align, defined as spin up ($|+\rangle$), or anti-align, defined as spin down ($|-\rangle$), with B_0 creating a two-level system. The distribution of $|\pm\rangle$ states are determined by the Boltzmann distribution, $\frac{N_+}{N_-} = e^{-\frac{\Delta E}{k_B T}}$. Here $N_\pm$ are the population in each energy state, ΔE is the energy difference ($E_{|+\rangle} - E_{|-\rangle}$), k_B is the Boltzmann constant ($1.1381 * 10^{-23}$ J/K), and T is temperature. As ΔE is a negative quantity and the argument of the exponential is greater than 1, the Boltzmann distribution dictates that the spins preferentially align with B_0 ($|+\rangle$). At equilibrium, the net magnetization vector $\mathbf{M}$ represents the macroscopic net magnetization of spins within the volume of interest, with M_0 being its maximum value. Due to the Zeeman effect, ΔE is directly proportional to B_0; therefore, increasing B_0 increases $\mathbf{M}$ and the available signal (M_0). Mathematically this is described by $M_0 = \frac{\hbar^2 \gamma^2 B_0}{4 k_B T} \rho_0$ where γ is the gyromagnetic ratio, $\hbar$ is the reduced Planck's constant ($1.055 * 10^{-34}$ J/s), and ρ_0 is the proton density. The gyromagnetic ratio (γ) is a fundamental physical constant that relates a nucleus's magnetic moment to its angular momentum. It determines the frequency (Larmor frequency: f_0) at which a specific nucleus (like hydrogen) precesses in a magnetic field (Larmor procession) as defined by $f_0 = \gamma B_0$. Each nucleus and isotope has a unique gyromagnetic ratio, making it a key factor in MRI's ability to distinguish between different substances. For hydrogen-1 (^{1}H), γ is 42.58 MHz/T. As common MRI field strengths are 1.5 and 3 T, these correspond to water Larmor frequencies of 63.87 MHz and 127.74 MHz, respectively. To receive signal, the MRI receiver coils are tuned to these specific frequencies.

Spatial encoding in MRI is achieved through gradients in the readout (frequency), phase, and slice directions, each with a unique function in defining image space. These gradients, which generate small magnetic field variations relative to B_0, encode location by inducing slight alterations in proton phase and Larmor frequency, the latter being directly proportional to magnetic field strength. This frequency shift is exploited during readout, allowing signal differentiation based on precession phase and frequency. Readout pulses then selectively "listen" for protons precessing at frequencies and phases that correspond to their position along the gradient. This process isolates signal originating from a specific spatial location.

These gradients operate across all three spatial dimensions. A gradient active during signal acquisition is designated a frequency-encoding gradient. This gradient spatially encodes protons along the readout direction by modulating the static magnetic field in that direction. While theoretically having unlimited resolution, the resolution is typically matched to the phase-encode direction. Within the same slice, orthogonal to the frequency-encode direction a phase-encoding gradient spatially encodes signal by varying precession phase according to proton position. Applied after the initial 90-degree RF pulse but before readout, these gradients temporarily alter B_0 in the phase-encode direction, causing a phase shift dependent on proton location. Finally, slice-selective gradients encode signal by exciting only those protons within the desired slice, ensuring that only these contribute coherent signal. This is accomplished by applying the gradient during the RF pulse, varying static B_0 strength across the slice-select direction, which allows the RF pulse to excite only protons within the frequency bandwidth corresponding to the selected slice [29, 30].

1.3.1 T_1-weighted and T_2-weighted Imaging

T1-weighted (T_{1w}) and T2-weighted (T_{2w}) scans correspond to the two types of relaxation processes within magnetic resonance spin systems: spin-lattice relaxation and spin-spin dephasing, respectively. Spin-lattice relaxation (T_{1w}) occurs when the system aligned to B_0 receives a perturbation in the form of another external magnetic field B_1. This perturbation causes spins to get 'knocked down' and undergo precession as they relax back to alignment with B_0. This relaxation emits a radio frequency (RF) signal that gets collected by the receiver coils. Spin-spin dephasing (T_{2w}) occurs during the spin-lattice relaxation process where net magnetization in the transverse plane, perpendicular to B_0, decays due to spin interactions with neighboring spins. Each process has a time associated with it; T_1 and T_2 relaxation times. Respectively, they represent the time taken to restore 63% and dephase 63% of the longitudinal and transverse signal. These times are characteristic of different tissues allowing for differentiation depending on the scan parameters repetition time (TR) and echo time (TE). TR is the time between RF pulses. For spin echo pulse sequences, TE is the time between the initial 90-degree RF pulse and the 180-degree followup RF pulse creating an 'echo'. This echo causes rephasing of spins and allows for stronger signal generation. As an example, a T_{1w} image provides excellent contrast between grey matter (GM) and white matter (WM) while a T_{2w} image provides tissue contrast based on water content. In general, a T_{1w} image uses a TR/TE combination of roughly 500/20 ms while T_{2w} is roughly 4000/100 ms [29,30].

1.3.2 Diffusion Weighted Imaging

Diffusion imaging uses MRI to measure the movement of hydrogen protons in water. While free water exhibits Brownian motion, tissue water diffusion is constrained by cell membranes. Because cell membranes impede water movement, areas with higher cell density and intracellular volume exhibit greater diffusion restriction, though recent perspectives challenge the validity of this premise. DWI employs diffusion gradients to track water molecule motion. A typical DWI sequence involves a 90-degree RF pulse, a 180-degree echo pulse, and diffusion gradients before and after the echo pulse. The first gradient encodes water molecule location. If a molecule moves significantly along the gradient direction between the two gradients, it dephases, reducing the signal. Conversely, limited movement leads to rephasing and signal detection. Consequently, increased diffusion correlates with greater signal loss as gradient strength increases. The b-value, determined by $b = \gamma^2 G^2 \delta^2 \left(\Delta - \frac{\delta}{3}\right)$, where gradient strength (G), diffusion gradient duration (δ), and diffusion gradient spacing (Δ), reflects the sensitivity of signal loss to water molecule motion. Higher b-values increase this sensitivity. Voxels with restricted diffusion retain more signal at higher b-values. An apparent diffusion coefficient (ADC) map, derived from the slope of the log(signal intensity) vs. b-value curve, displays unrestricted diffusion as brighter and restricted diffusion as darker [29].

1.4 Positron Emission Tomography

PET is a widely used imaging technique for tumor staging due to its ability to probe metabolic activity. While effective, PET's spatial resolution of approximately 5 mm and complex logistics involving radiotracer production, shipping, shielding, patient uptake, and waste management has limitations. PET imaging relies on the principles of matter-antimatter annihilation. Specifically, a positron-emitting radiotracer administered to the patient decays, releasing a positron (β^+ particle). This β^+, the antimatter of an electron, interacts with an electron, resulting in their annihilation and the production of two 0.511 MeV photons. These photons are emitted approximately 180 ± 0.5 degrees relative to each other. The detector system of PET then discriminates detection events based on coincidence timing along a line of response. Newer systems allow time-of-flight considerations which allow for greater spatial resolution.

To capture and enhance signals, PET scanners rely on scintillation detectors linked to photomultiplier tubes (PMTs). The visible light emitted by these scintillators is transformed into electrons by a photocathode within the PMTs. These electrons are then accelerated and multiplied as they traverse toward the anode, where the accumulated charge is converted into an electrical signal. Scintillation materials in PET, each with unique advantages and disadvantages, can include NaI(Tl), BGO, LYSO, or GSO. Crystal dimensions are specifically designed to interact with the 0.511 MeV photons characteristic of PET. As compared to X-ray systems, which utilize lower-energy photons, PET requires thicker crystals.

^{18}F-FDG-PET is a widely utilized imaging modality in oncology, fundamentally based on the Warburg effect. The Warburg effect describes the metabolic shift in cancer cells towards increased glucose uptake and glycolysis, even in the presence of oxygen, which is atypical for normal cells. ^{18}F-FDG, a glucose analog, is actively transported into these cells and trapped intracellularly, reflecting their elevated glucose metabolism. This metabolic characteristic makes ^{18}F-FDG PET a valuable tool for tumor detection, staging, and monitoring treatment response across various cancer types, although its specificity can be limited in certain tissues, such as the brain, where normal glucose metabolism is also high [27].

To provide quantitative information on radiotracer uptake, the use of standard uptake values (SUV) are used. SUV allows for the conversion of measured activity from the PET system to a per tissue uptake following the Equation 1.1 [30, 31].

$$\text{SUV} \left[\frac{g}{mL}\right] = \frac{\text{Activity Concentration } \left[\frac{\text{Bq}}{\text{mL}}\right] * \text{Patient Weight [g]}}{\text{Decay Adjusted Injected Activity [Bq]}} \tag{1.1}$$

Accurately differentiating tumor recurrence from treatment-related changes (TRC), such as pseudoprogression and radiation necrosis, remain a significant challenge in glioma management as these conditions often mimic recurrent tumor on standard MRI [32–35]. Although FDG-PET offers modest utility in this distinction, its extensive uptake in normal brain tissue and increased signal in inflammatory regions severely diminish its specificity and tumor-to-background ratio in neuro-oncology [33–35]. Conversely, amino acid PET tracers, such as ^{18}-fluoroethyl-tryosin (FET) and L-[Methly-^{11}C]-Methionine (MET), have demonstrated elevated capabilities in distinguishing TRC from recurrence by more precisely targeting tumor metabolism. Due to their improved performance, amino acid PET has begun being clinically implemented.

1.5 Motivations for MADI

The current state of in vivo metabolic imaging is based on radiotracers which have resolution, accessibility, and radiation safety limitations; in contrast MRI does not have these limitations. For MADI, we aspire to probe in vivo cellular metabolic activity using imaging biomarkers, $k_{io}V$ and $k_{io}V\rho$, as an alternative to radiotracer imaging such as in PET. Beyond biomarkers, MADI provides additional parameters (k_{io}, ρ, V, and v_i) which may provide valuable information for grading and staging gliomas.

1.6 Project Goals

This Thesis aimed to achieve three primary objectives: first, to assess MADI's ability to differentiate normal tissue from tumor and pseudoprogression; second, to compare MADI's established ability to the common MA imaging FDG-PET; and third, to identify limitations within MADI's current implementation.

Chapter 2

Methods

2.1 Population

The human studies were conducted on informed and consenting participants inline with the project design approved by the Oregon Health & Sciences (OHSU) Institutional Review Board (IRB). Participants were eligible if they had glioma and were undergoing a PET-MR exam. Due to current OHSU protocols, this restricted the population to participants who have undergone tumor resection. All participant data was anonymized and stored in a Microsoft OneDrive folder. Table 2.1 contains participant tumor type and radiologist determined response assessment: tumor progression (tumor) or pseudoprogression. For the pseudoprogression population, subsequent followup imaging was radiologist-evaluated for conformation of progression status. To assess progression, radiologist utilize various imaging techniques: T1pre, T1post, PET, ADC, cerebral blood volume (CBV), cerebral blood flow (CBF), arterial spin labeling (ASL), and dynamic susceptibility contrast (DSC). They also rely on established literature like the Response Assessment in Neuro-Oncology (RANO) criteria for MRI and amino acid PET.

Participant #	Tumor Type	Progression
1388	Glioblastoma	Pseudo
1803	Glioblastoma	Tumor
1820	Oligodendroglioma	Pseudo
1950	Glioblastoma	Tumor

Table 2.1 Collection of participants' tumor type and designation of tumor or pseudoprogression.

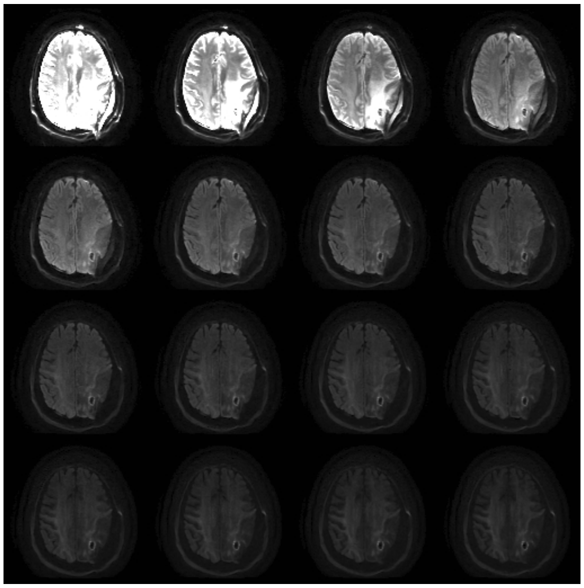

Figure 2.1 A single slice of a spin echo DWI image of participant 1388. Image contains b values 50, 360, 670, 980, 1290, 1600, 1910, 2220, 2530, 2840, 3150, 3460, 3770, 4080, 4390, and 4700 s/mm^2.

2.2 Image Acquisitions

All images were acquired on a GE Signa PET/MR system featuring a 3.0 T MRI and time of flight (TOF) PET imaging. The 2 dimensional spin echo DWI was acquired with the following parameters: FOV of 24.0 cm x 24.0 cm, voxel dimensions of 0.9375 mm x 0.9375 mm x 3.3 mm, 46 slices, TR of 4256 ms, TE of 111.5 ms, and b values of 50, 360, 670, 980, 1290, 1600, 1910, 2220, 2530, 2840, 3150, 3460, 3770, 4080, 4390, and 4700 s/mm^2. Recon-DL was used for denoising. Figure 2.1 depicts a single slice of a DWI image across each 16 b values. The T$_{1w}$ scans were acquired using MP-RAGE sequence with the following parameters: FOV of 24.0 cm x 24.0 cm, voxel dimensions of 0.5 mm x 0.5 mm x 0.5 mm, a range of 344 to 376 slices, TR of 7.7 ms, TE of 3.1 ms, inversion time 417 ms, flip angle of 8.0 degrees. The T_{1w} post-gadolinium contrast (T1post) scan, used Gadoterate Meglumine 0.5 mmol/mL contrast. Figure 2.2 depicts slices of a T1post image. The PET scans were acquired with voxel dimensions 1.17 mm x 1.17 mm x 2.78 mm. Each participant was injected with 7.25 to 8.91 mCi of ^{18}F-FDG intravenously and were imaged 45 to 60 minutes post-injection. Figure 2.3 depicts slices of a ^{18}F-FDG-PET image.

2.3 MADI Map Creation

The MADI maps are generated using raw DWI images spanning b values 50, 360, 670, 980, 1290, 1600, 1910, 2220, 2530, 2840, 3150, 3460, 3770, 4080, 4390, and 4700 s/mm^2. On a per voxel basis, the b value decay is compared to a library of curves for k_{io}, ρ, V, and v_i and matched to best fit. The best fit is found computing the $\min_i \left|\left| \frac{s_x}{s_{x,0}} - \frac{l_i}{l_{i,0}} \right|\right|$ where s_x is the signal intensity at $b = x$, $s_{x,0}$ is the signal intensity at $b = 0$ s/mm^2, i is the iteration of the library being compared to, l_i is the library value at $b = x$, and $l_{i,0}$ is the library value at $b = 0$ s/mm^2. Figure 2.4 is an example of each MADI map for participant 1388.

The library curves were generated by Monte-Carlo random-walk simulations computed on water-filled, water-immersed, randomly-size, and randomly-shaped Voronoi cells with a key assumption that the main barrier of diffusion are the cell membranes [1, 15].

Beyond MADI, various advanced DWI approaches have been developed to quantitatively characterize cellular volume and size within heterogeneous biological tissues. These techniques commonly employ specialized acquisition schemes, typically com-

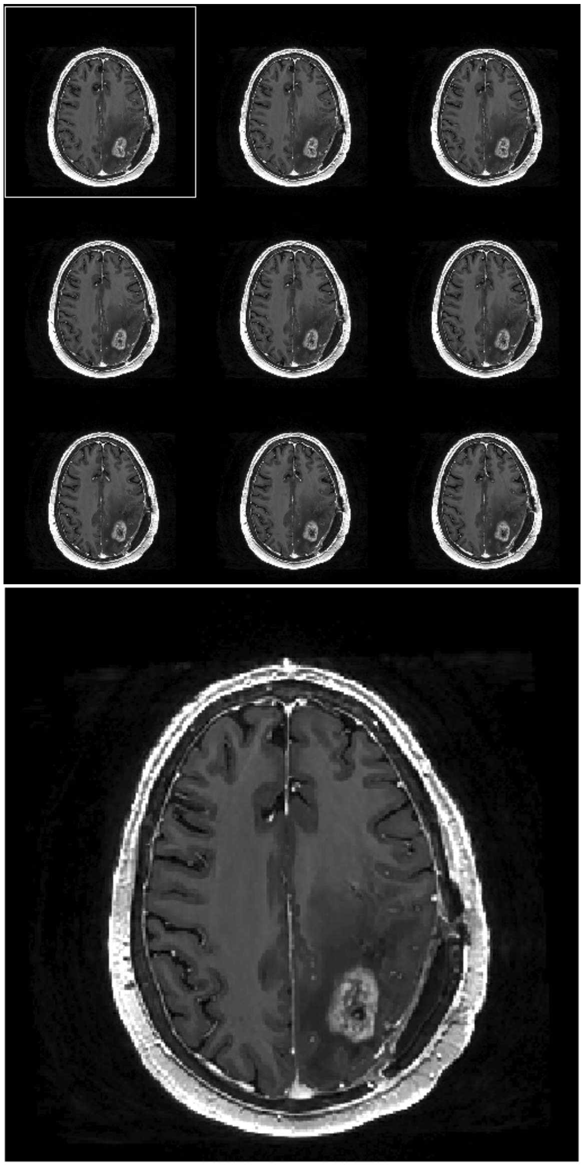

Figure 2.2 (Top) Slices of a T1post image of participant 1388. (Bottom) Individual slice from participant 1388's T1post image.

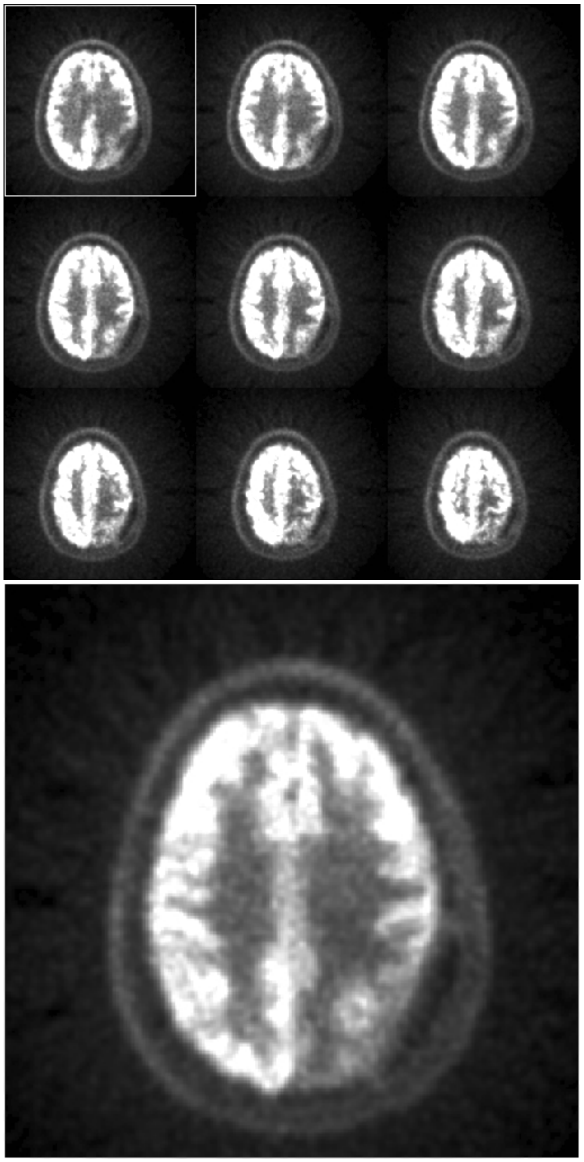

Figure 2.3 (Top) Slices of a ^{18}F-FDG-PET image of participant 1388. (Bottom) Individual slice from participant 1388's ^{18}F-FDG-PET image.

bining pulsed gradient spin echo (PGSE) and oscillating gradient spin echo (OGSE) DWI scan protocols. A common assumption in many of these models is a simplified spherical cell geometry, which, while offering computational simplicity, may not fully capture the irregular morphology prevalent in many biological cell population [36–39]. In contrast to these approaches, MADI separates itself by incorporating a more sophisticated microstructure model with the random-size and randomly-shaped Voronoi cell structure which better models the diverse cellular shapes and packing arrangements found in tissue. Unlike MADI, which can quantify metabolic parameters, e.g., k_{io}, these various DWI approaches do not possess this capability.

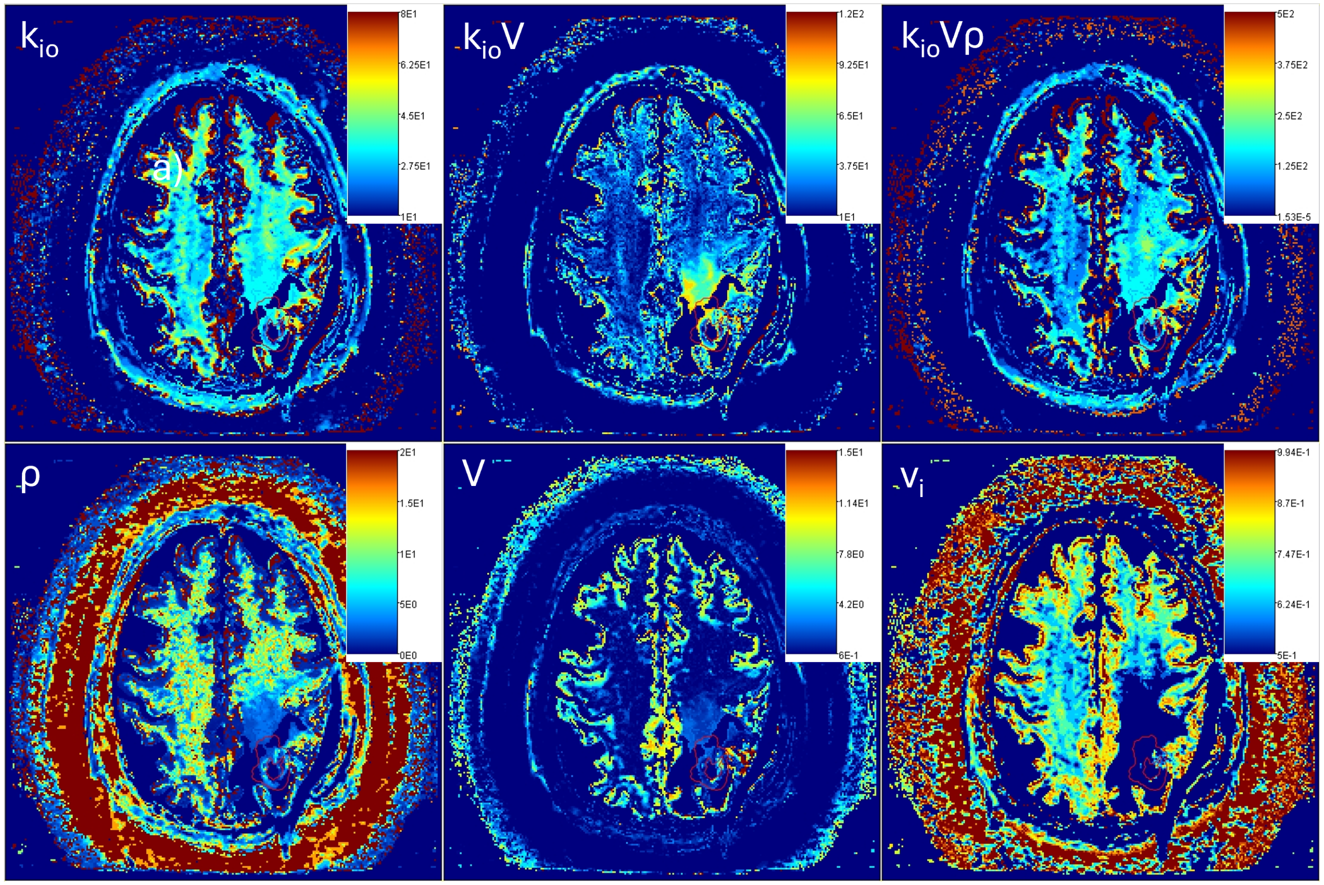

Figure 2.4 A Slice of maps of all MADI parameters of participant 1388: a) k_{io} [1/s], b) $k_{io}V$ [pL/s/cell], c) $k_{io}V\rho$ [10^5 pL/s/μL], d) ρ [10^5 cells/μL], e) V [pL/cell], and f) v_i [1]. pROI-Hollow is outlined in red. Images depicted underwent 20 pL/cell filtering.

2.4 Image Registration

Using Xinapse Systems Ltd Jim 9's image registration tool, all images were registered together and manually inspected. Each image was registered to an ADC map. As both ADC and MADI maps were generated from DWI images, no registration was required. The PET and T_{1w} pre-gadolinium contrast (T1pre) images were registered directly to the ADC map and the T1pre transform file was saved. T1post was registered to the unregistered T1pre, inspected, and then had the T1pre transform file applied.

2.5 Image Analysis

2.5.1 Regions of Interest

The primary region of interest (pROI) was defined to be the location of T1post enhancement signifying a region of tumor or pseudoprogression. As seen in Figure 2.5, three different subsets of pROI were created: the entirety of the region contained within the perimeter of the T1post enhancement, a more central T1post non-enhancing region, and only the T1post enhancement. These regions will be referred to as the entire, core, and hollow ROIs, respectively. The pROI ranges over multiple slices within an image.

For the control data, ROIs were created on either the T1pre or T1post images. The half-brain contralateral ROI encompasses the contralateral side of the cerebrum to the pROI. Spatially direct contralateral ROIs were avoided as they're susceptible to variation in tissue composition. Additionally, resection can affect how the brain occupies space within the skull reducing the symmetry on both sides and accuracy of direct contralaterals. GM and WM ROIs were created on the contralateral side of the brain on an image slice that is most conducive to ROI creation.

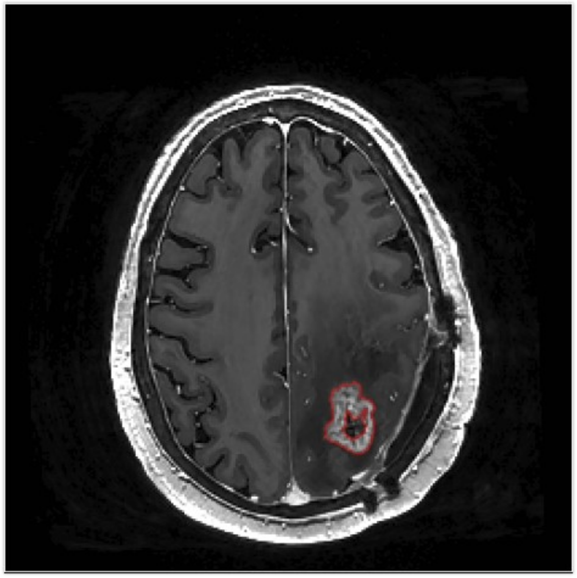

Figure 2.5 Participant 1388's T1post image with pROI regions depicted.

All ROIs were generated using the 'ROI Analysis' toolkit within Xinapse Systems Ltd Jim 9 using the 'contour following' function with 'Pixel Snap' deactivated. Manual edits were made on a case-by-case basis.

For PET, using the Xinapse Systems Ltd Jim 9 ROI function 'Dilate', an ROI of pROI-Entire's local surroundings were created. This included three ROI dilation operations and was performed to quantify the pROI's local PET enhancement.

2.5.2 Data Collection

Each ROI was applied to each image and a printout of pixel intensity was generated using Xinapse Systems Ltd Jim 9 as a .txt file. The organization of the .txt files have columns corresponding to pixel location and their intensity. These .txt files were compiled into Microsoft Excel spreadsheets.

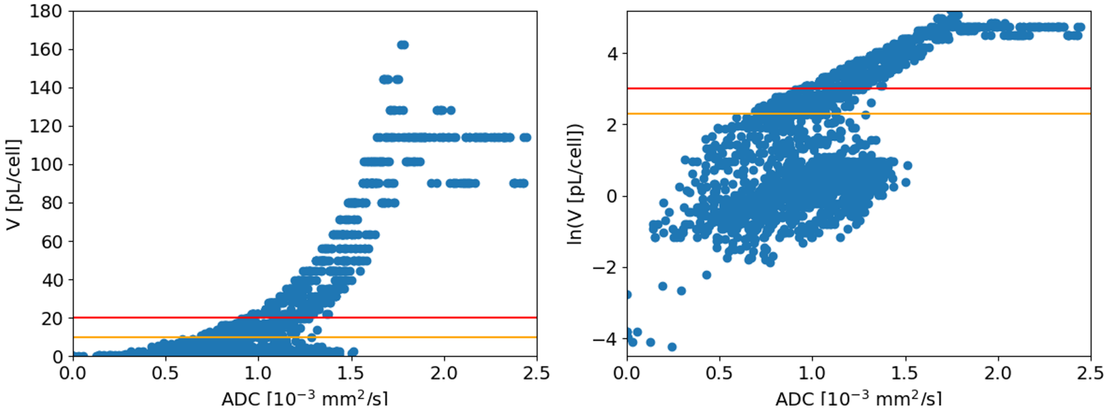

Figure 2.6 Plots of ADC vs V on linear (left) and logrithmic (right) scales demonstrating scope of ill-fitting pixels. Orange and red line corresponds to 10 and 20 pL, respectively. Bifunctional behavior of data shown; exponential-like and linear-like. Data is reflective of participant 1950.

2.5.3 Data Processing

Using Python 3.9.13, codes were created to import, process, and export data. The following Python packages were used: NumPy 1.21.0, Matplotlib 3.4.2, pandas 1.3.0, SciPy 1.7.0.

For all MADI-based datasets it was necessary to perform two layers of data filtration. First, each pixel passed through a volume filter where if cellular volume was greater than 20 pL/cell it was removed from the dataset. As seen in Figures 2.6, A.1, A.2, and A.3 there exists a systematic ill-fitting of voxels with cellular volumes reaching up to 180 pL. From previous MADI imaging, the median cellular volumes of cortical GM and WM were found to be 6.0 and 0.91 pL/cell, respectively [1]. There appears to be two distinct functions contained within the data: an exponential-like function containing the non-physical points and a linear-like function assumed to be true uncorrupted data. As a result, a 20 pL threshold was found to be sufficient to preserve all true data, remove as much ill-fitted points, and maintain availability for possible large cell volume to be included. An additional feature the 20 pL filter had was removal of all cerebrospinal fluid (CSF) spaces contained within ROIs. The second filter applied to MADI data was to remove extreme outliers that don't get removed with the 20 pL filter by taking only the 0^{th} to the 95^{th} percentiles. This became crucial in assuring the Kullback-Leibler divergence worked properly.

Using SciPy, a gaussian kernel density estimation (KDE), using Scott's rule for bandwidth, was calculated on each parameters dataset to produce an unnormalized probability density function (PDF). PDFs behave similar to histograms, but without the impact of bin width and allow for the transformation of a discrete set to an estimated continuous set [40].

2.5.4 Kullback-Leibler Divergence

The Kullback-Leibler (KL) divergence primarily has its applications in information and computer sciences. As an example, in machine learning the KL divergence is used for its utility in comparing models and evaluating performance. Currently, there have been no applications of KL divergence for direct image analysis, constituting a novel method of analysis. For normally distributed dataset, a mean and standard deviation may be sufficient to fully characterize the dataset. Once a distribution starts to become skewed or multi-modal, the characterization becomes more challenging. This is where the strength of the KL divergence lies; its ability to compare the entirety of a distribution. The KL divergence is defined by Equation 2.1, where $p(x)$ is a normalized PDF that $q(x)$, another normalized PDF, is being compared to and $\{x_{min}, x_{max}, dx\}$ describes the parameter grid being integrated over.

$$\text{Relative Entropy [nat]} = \int_{x_{min}}^{x_{max}} p(x) \ln\left(\frac{p(x)}{q(x)}\right) dx \tag{2.1}$$

For MADI-based data, the parameter grid per parameter was constructed to range

Parameter	Minimum	Maximum	Step Size
k_{io} [1/s]	0	120	0.1
$k_{io}V$ [pL/s/cell]	0	150	0.1
$k_{io}V\rho$ [10^5 pL/s/uL]	0	800	0.1
ρ [10^5 cells/uL]	0	25	0.01
V [pL/cell]	0	12	0.01
v_i [1]	0.5	1	0.001

Table 2.2 Characterization of parameter grids use for normalization and KL divergence calculations.

from 0 to the maximum value across all datasets in step sizes of a thousandths of the maximum value's order of magnitude, see Table 2.2. v_i used a minimum value of 0.5 as that is MADI's current lowest limit. For PET-based data, the parameter grid was constructed to range from the minimum to the maximum value across a participant's dataset in step sizes of a thousandths of the order of magnitude of the maximum value. All unnormalized PDFs were normalized over their parameter grid. The method of integration performed used the trapezoidal rule. To assess and group participant data by a single PDF, averaged PDFs were used. To calculate this, at each point in the parameter grid the mean of each participant's PDF value (grouped by progression status or all together) was taken.

The KL divergence is a statistical distance which outputs a measure of relative entropy (RE) in natural units. This value is always positive and can be likened to a likelihood or surprise factor. If RE is zero, then both distributions are the same. The larger RE gets, the more $q(x)$ differs from $p(x)$. RE does not have an absolute scale to compare against, but rather is used to compare two different PDFs to the same $p(x)$. This is a critical condition: the consistency of $p(x)$. Suppose two measurements of RE were made, RE_i and RE_j. In order to compare RE_i and RE_j to each other it necessitates that $p_i(x) \simeq p_j(x)$.

Measures of RE were averaged together based on tumor and pseudoprogression diagnosis quoted with a standard error (SE).

2.6 PET

As determined in Section 3.2.2 with Figure 3.6, PET is ineligible for KL divergence analysis. To analyze the images, measurements of degree of enhancement were made instead. Given the approximately normal distribution of the data, the mean and standard deviation were used to characterize its distribution. To quantify local enhancement visible in the images, a ratio of $\mathrm{SUV_{mean}}$ of the pROI-Entire to its surroundings was calculated. To quantify global enhancement, the ratio of $\mathrm{SUV_{mean}}$ of the pROI-Entire to contralateral GM was calculated. Error was propagated in quadrature.

2.7 Water Glucose Index

The water glucose index (WGI), a ratio of cellular metabolic rates of active water cycling (${}^{c}\mathrm{MR_{AWC}}$) and glucose uptake (${}^{c}\mathrm{MR_{glc}}$), is a measure of shifts in energy production between oxidative phosphorylation and glycolysis. $k_{io}V$ is a direct measure of ${}^{c}\mathrm{MR_{AWC}}$ $[\mu\mathrm{L_{water}/s/cell}]$. Using a conversion factor, SUV can become a measure of metabolic rate of glucose uptake per tissue (${}^{t}\mathrm{MR_{glc}}$) by ${}^{t}\mathrm{MR_{glc}}\ \left[\mathrm{pmol_{glc}}/\mathrm{s}/\mu\mathrm{L_{tissue}}\right] = 3.2 * \mathrm{SUV_{max}}$ [41]. Dividing by ρ $[\mathrm{cells}/\mu\mathrm{L_{tissue}}]$, ${}^{t}\mathrm{MR_{glc}}$ becomes ${}^{c}\mathrm{MR_{glc}}$. For computation of WGI, the following equation was used,

$$\mathrm{WGI}\ \left[\mu\mathrm{L_{water}}/\mathrm{pmol_{glc}}\right] = \frac{\mathrm{med}\,(k_{io}V)\ \ [\mu\mathrm{L_{water}/s/cell}] * \mathrm{med}\,(\rho)\ \ [\mathrm{cells}/\mu\mathrm{L_{tissue}}]}{3.2 * \mathrm{SUV_{max}}\ [\mathrm{pmol_{glc}}/\mathrm{s}/\mu\mathrm{L_{tissue}}]} \tag{2.2}$$

where $\mathrm{med}(k_{io}V)$ represents the median of $k_{io}V$. WGI is an example of how MADI can couple with other imaging to provide additional information. Here, MADI couples with FDG-PET to create a measure of how cellular metabolism biases to either oxidative phosphorylation and aerobic glycolysis, probed by active water cycling and glucose uptake respectively.

Chapter 3

Results

3.1 Control Data

3.1.1 Grey and White Matter

As MADI is still a novel approach with little data on human brains, data on GM and WM was collected to verify results. Figure 3.1, compares collected data to existing data. In previous healthy human brain data, cellular volumes for WM were found to be fairly localized around 0.9 pL while GM was bimodal with a localized peak at roughly 0.5 pL and a broad distribution from 3 to 12 pL. In measurements made from contralateral tissues, the same distributions were observed. The WM peaks were centered within 0.5-1.0 pL and GM showed bimodal behavior around 0.5 and 9 pL.

The differences in GM and WM distributions suggest there should be some degree of visual differentiation between each tissue using a cellular volume map. By using a T1pre image, which provides excellent soft tissue contrast, direct comparison of regions can be made. In Figure 3.2, cellular volume is visually less enhancing in WM than most regions within GM.

KL divergence was calculated to quantify the difference between GM and WM on

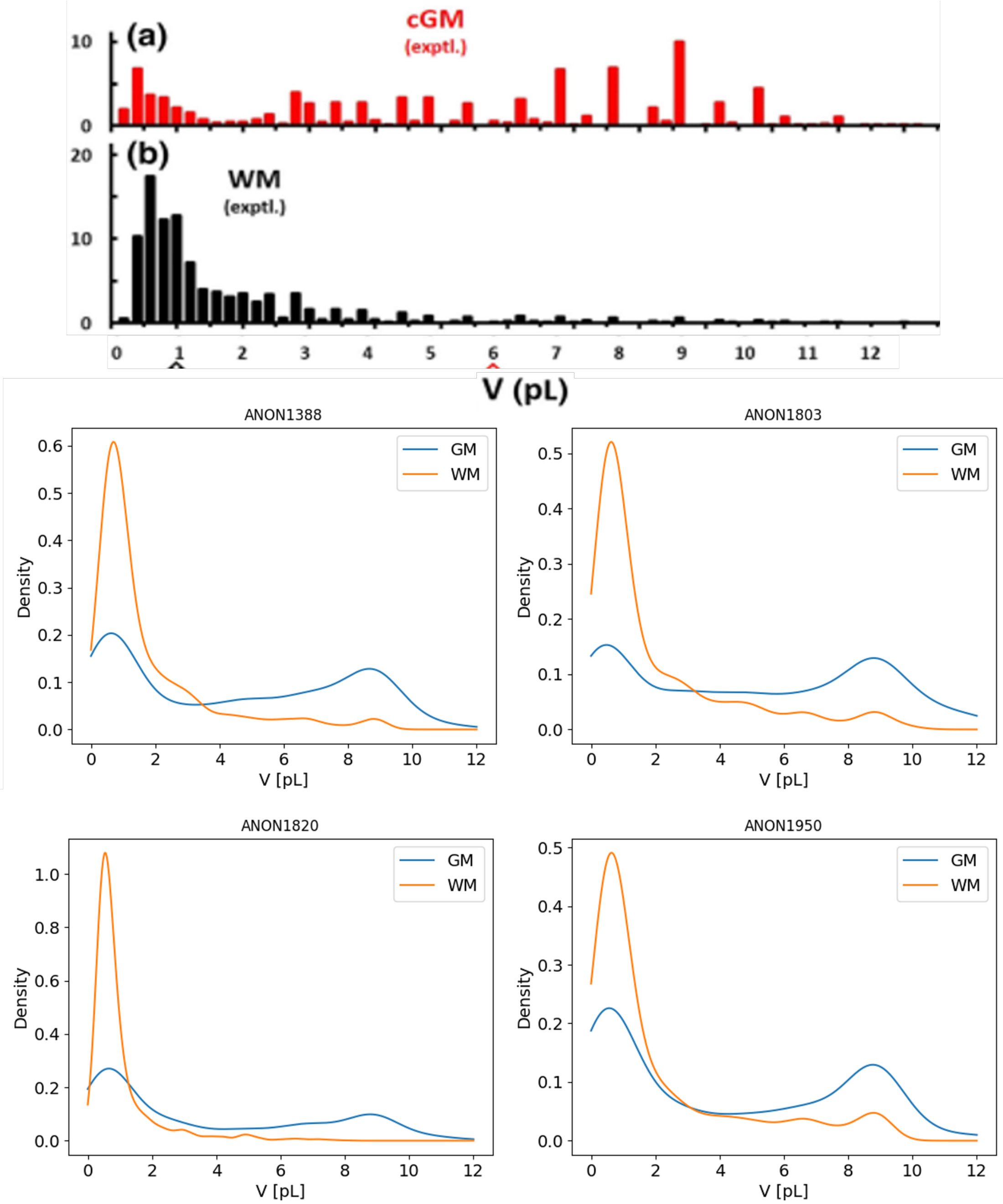

Figure 3.1 Comparison of GM and WM distributions from modified Figure 5 of Springer et al [1] (top) and each participant's contralateral (bottom).

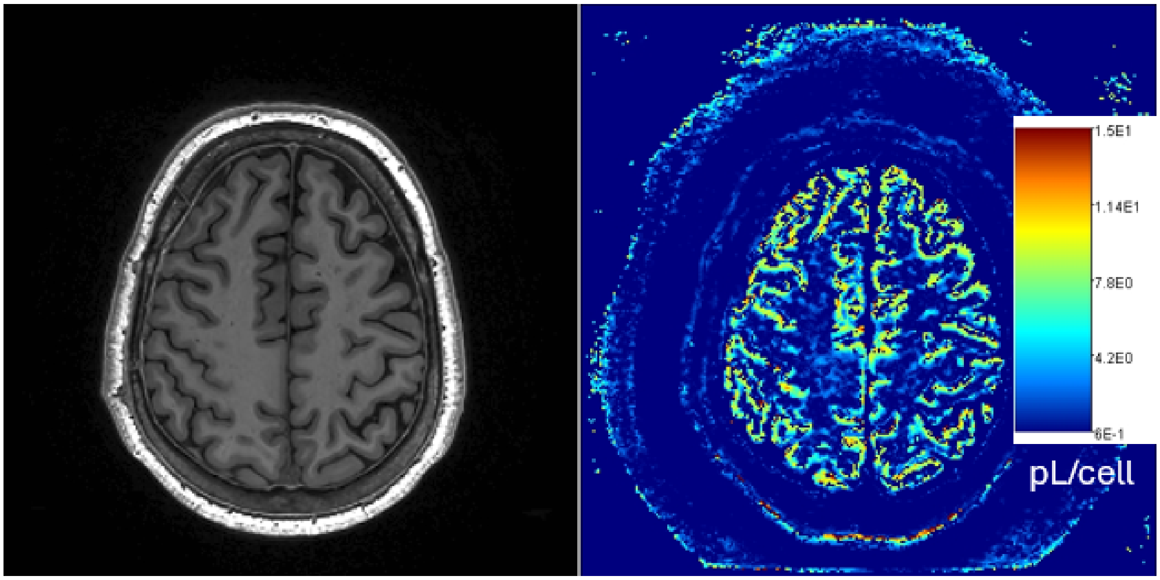

Figure 3.2 Comparison of a T1pre (left) and V (right) image for visual differentiation of GM and WM.

a per participant basis. The RE values per participant were averaged together and presented in Figure 3.3. For cellular volume, RE was found to be third highest of all MADI parameters with a value of 0.454 ± 0.236 nat.

3.1.2 $p(x)$ Consistency

In order to use KL divergence, establishing consistency of the comparison PDF is needed. Figure 3.4 contains the summary of the average RE of half-brain control per participant to the average half-brain PDF for MADI. The best case (lowest RE) parameter is ρ at 0.00228 ± 0.00163 nat and the worst case (highest RE) parameter $k_{io}V$ at 0.0160 ± 0.0076 nat. figure 3.5 shows the best and worst case sets of comparison PDFs. Visually, the difference in distributions aligns with ρ being a more consistent set of PDFs in comparison to $k_{io}V$.

The same process was performed for PET. In Figure 3.6, visually it is clearly demonstrated that the comparison PDFs are not consistent and thus PET is ineligible

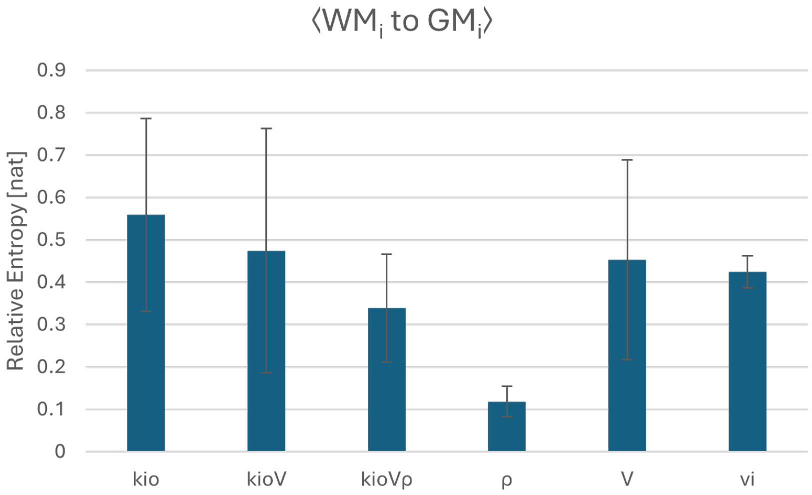

Figure 3.3 The average RE of per participant WM to GM distributions.

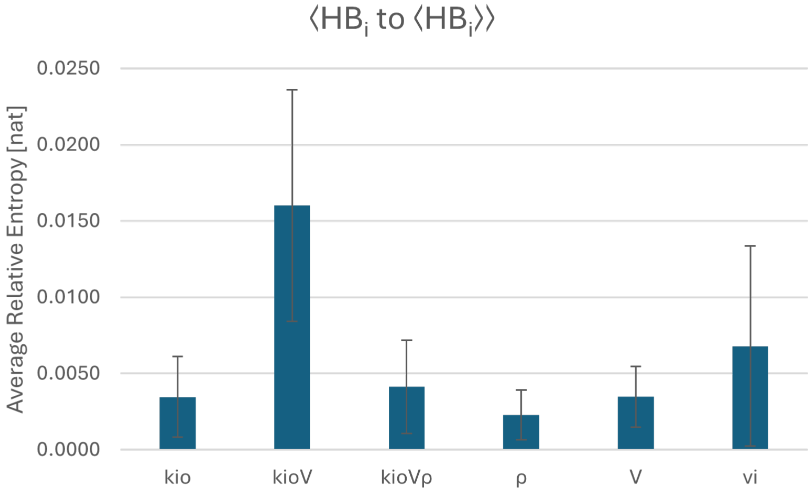

Figure 3.4 The average RE of per participant half-brain contralateral PDF to the population's average PDF.

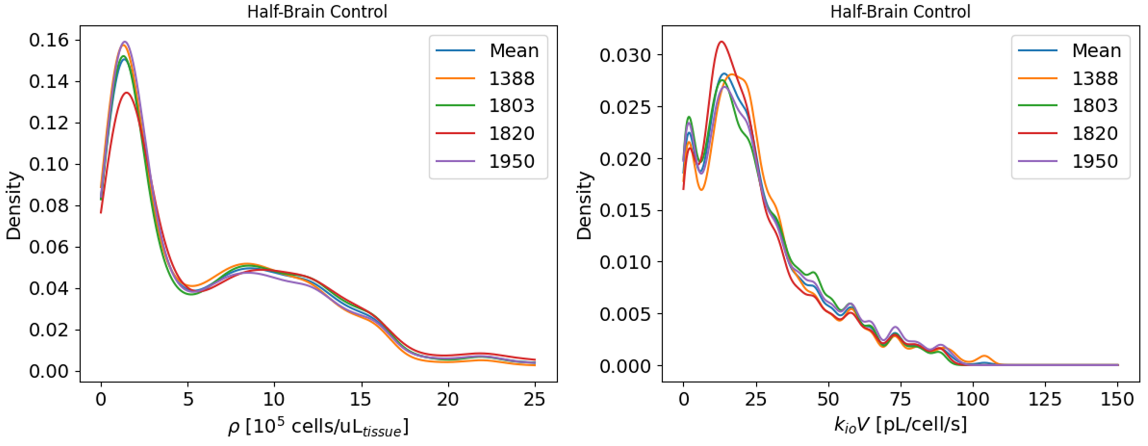

Figure 3.5 Comparison of per participant half-brain contralateral PDF to population averaged PDF. ρ (left) is the lowest RE parameter while $k_{io}V$ (right) is the highest.

for KL divergence analysis. The average RE was calculated to be 0.798 ± 0.433 nat.

3.2 MADI

3.2.1 pROI Selection

The KL divergence was calculated across the three different pROIs to their HBCL and then averaged by progression status. Using Figure 3.7 it was decided to use just the Entire pROI as in some participants it was too difficult to define a Core ROI, the Entire and Hollow pROIs were similar to each other, and simplicity of ROI creation.

3.2.2 Tumor & Pseudoprogression & Half-Brain

The KL divergence was calculated for the Entire pROI to HBCL for each participant and averaged by progression status. As seen in Figure 3.8, the RE is on the order of magnitude of 0.1 to 10 nat with V showing the greatest difference between both

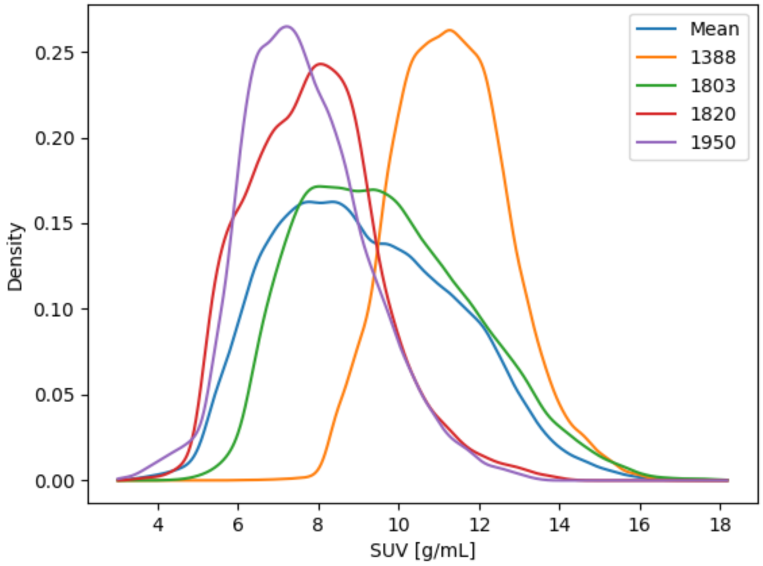

Figure 3.6 Comparison of per participant GM contralateral PDF to population averaged PDF.

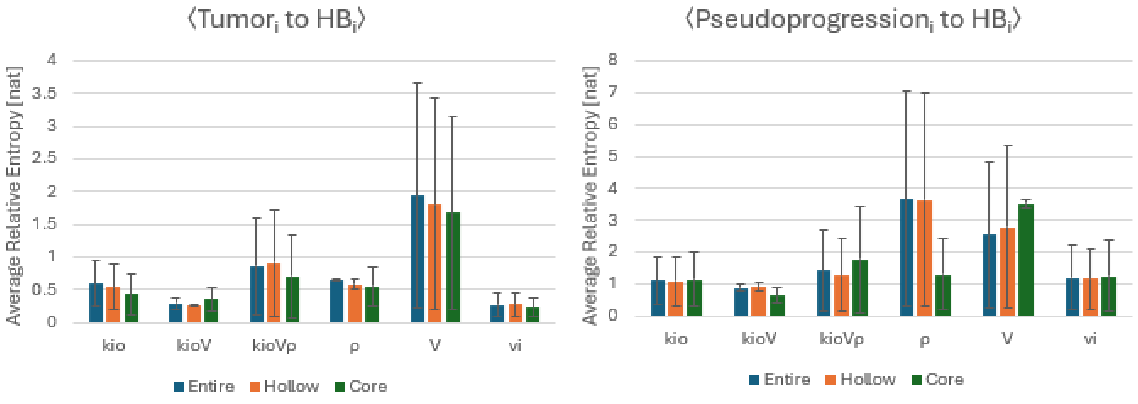

Figure 3.7 The grouped population's average RE of pROI to HBCL. Tumor group (left), pseudoprogression group (right).

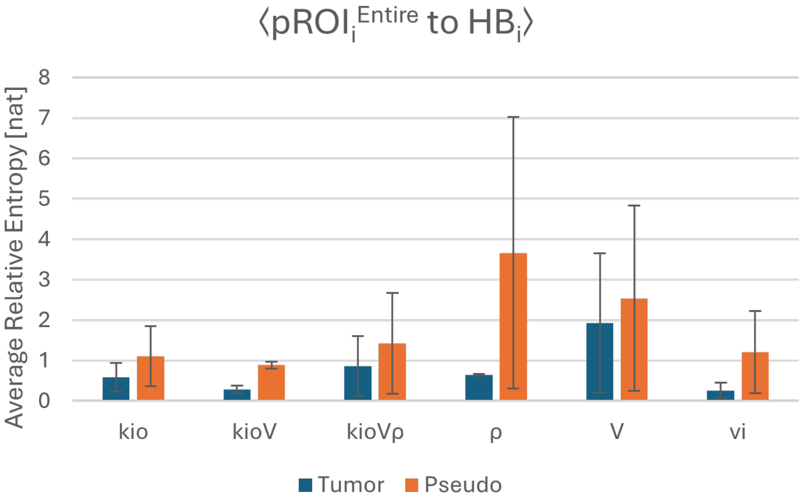

Figure 3.8 The grouped population's average RE of pROI-Entire to half-brain contralateral.

groups and their HBCL. Additionally, ρ has the greatest difference between tumor and pseudoprogression REs. Accounting for error bars, while $k_{io}V$ may have some of the lowest pROI to HBCL, there is no overlap between groups. The REs for $k_{io}V$ tumor and pseudoprogression are 0.293 ± 0.093 nat and 0.891 ± 0.088 nat, respectively.

As seen in Figure 3.9, by directly comparing the tumor and pseudoprogression groups both $k_{io}V$ and ρ show the greatest RE at 0.151 and 0.173 nat, respectively. The parameter with the smallest RE, 0.0860 nat, was k_{io}. The order of magnitude for RE across all parameters was about 0.1 nat.

Figure 3.10 shows the weakest and strongest parameter for pROI to HBCL and tumor to pseudoprogression differentiation. For $k_{io}V$, the three PDFs are fairly distinct and moderately separated. On median, there is roughly 20 pL/s/cell differentiation between each distribution. In contrast, k_{io} only provides roughly 15 1/s separation between pROI and HBCL, but absolutely no differentiation between tumor and pseudoprogression.

As a more rudimentary but accessible representation of the dataset, averaged

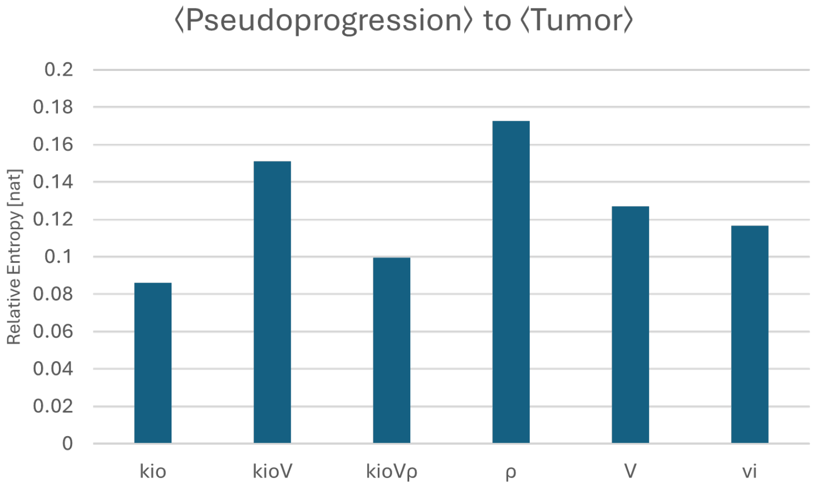

Figure 3.9 The RE of the averaged pseudoprogression PDFs to the averaged tumor PDFs for pROI-Entire.

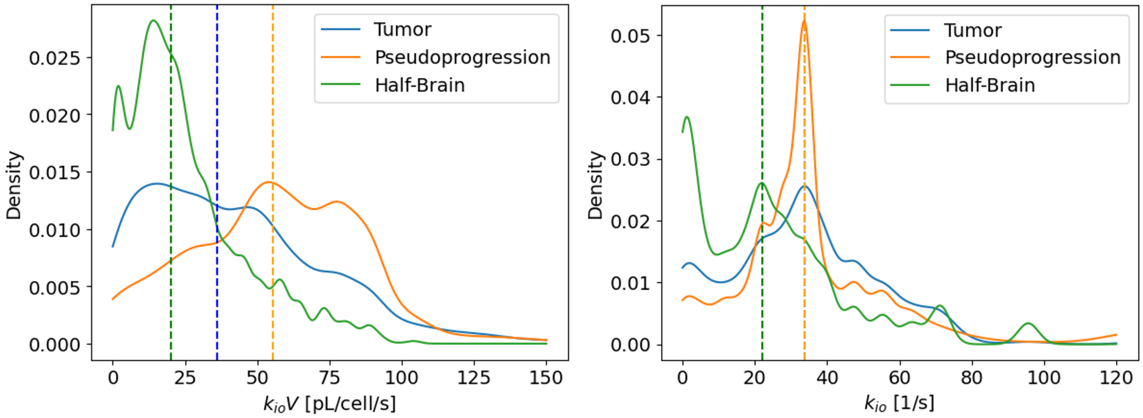

Figure 3.10 Plots of group averaged PDFs for $k_{io}V$ (left) and k_{io} (right) to represent the weakest and strongest cases for tumor-pseudoprogression-halfbrain differentiation. Vertical dashed lines represent each PDF's median value.

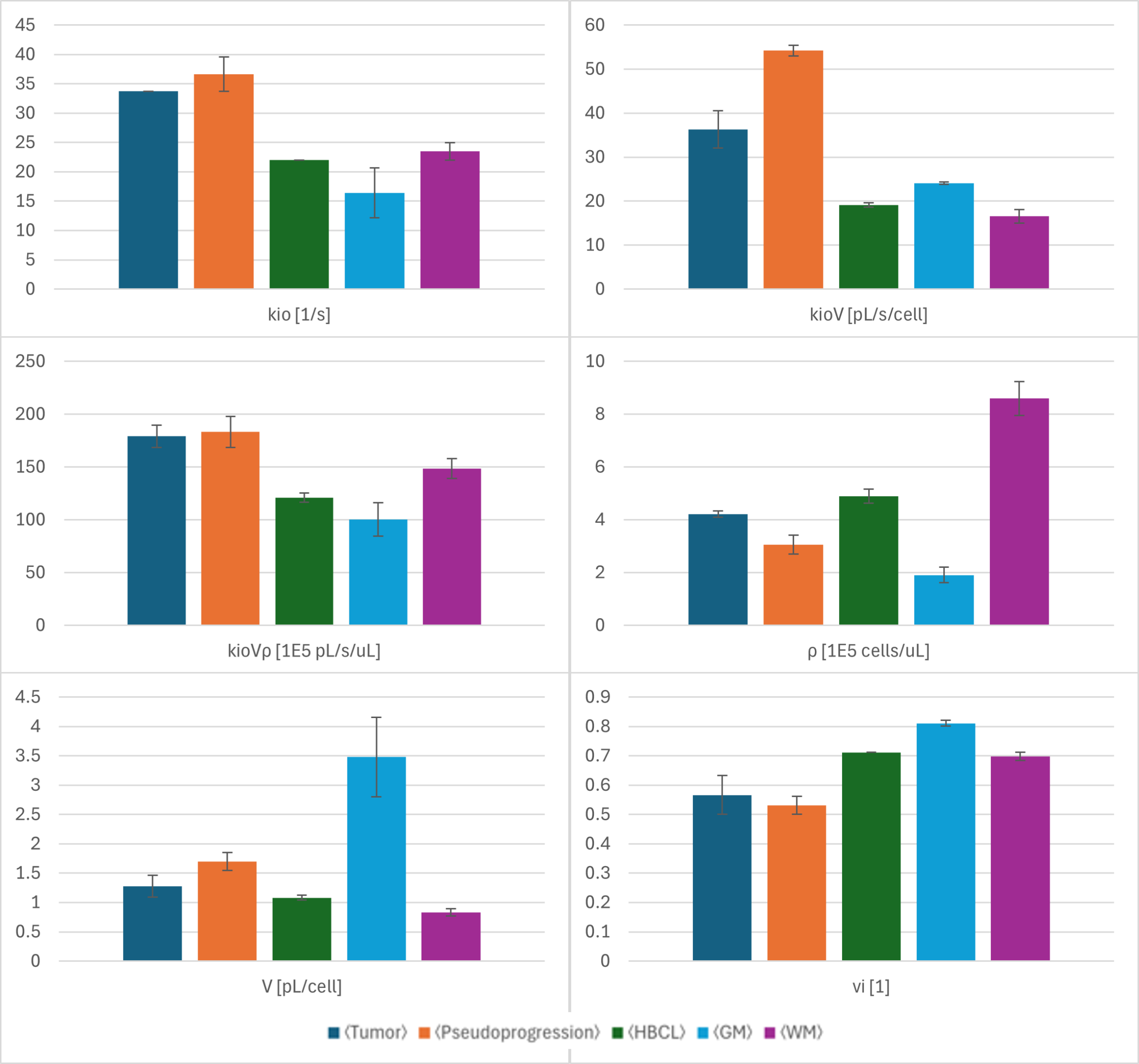

Figure 3.11 Plots of averaged medians with SE for all MADI parameters.

medians with SE for each MADI parameter across all ROIs were collected and plotted in Figure 3.11.

3.3 PET

Figure 3.12 depicts the quantification of the Entire-pROI relative enhancement present in PET imaging. All pROIs had greater SUV$_{\text{mean}}$ than their local surroundings (ranging from 7% to 30% increase), but there was less uptake than in GM (ranging from

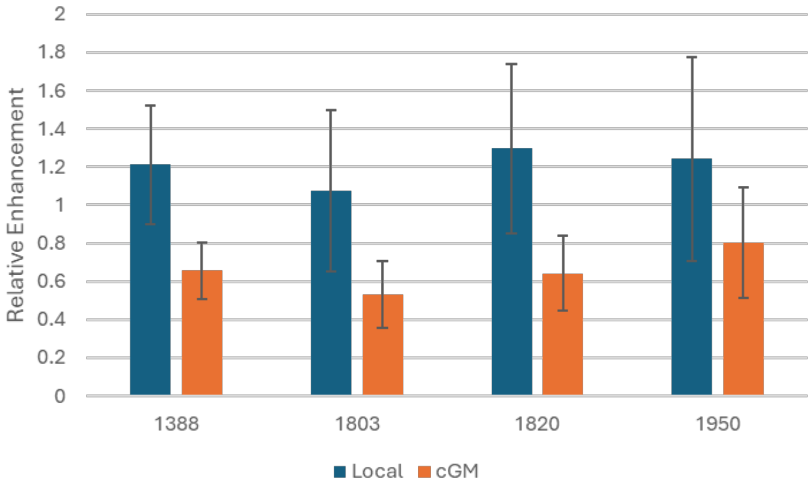

Figure 3.12 The relative enhancement ($\mathrm{SUV}_{\mathrm{mean}}^{\mathrm{pROI}}/\mathrm{SUV}_{\mathrm{mean}}^{\mathrm{comparison}}$) occurring within each participant's PET image.

20% to 66% decrease). No trend observed between tumor and pseudoprogression groups.

3.4 WGI

Figure 3.13 looks at the type of MA occurring within the Entire-pROI, GM, and WM for each participant. Per the same glucose uptake, the Entire-pROI had elevated transcytolemmal water efflux to GM, but decreased to WM.

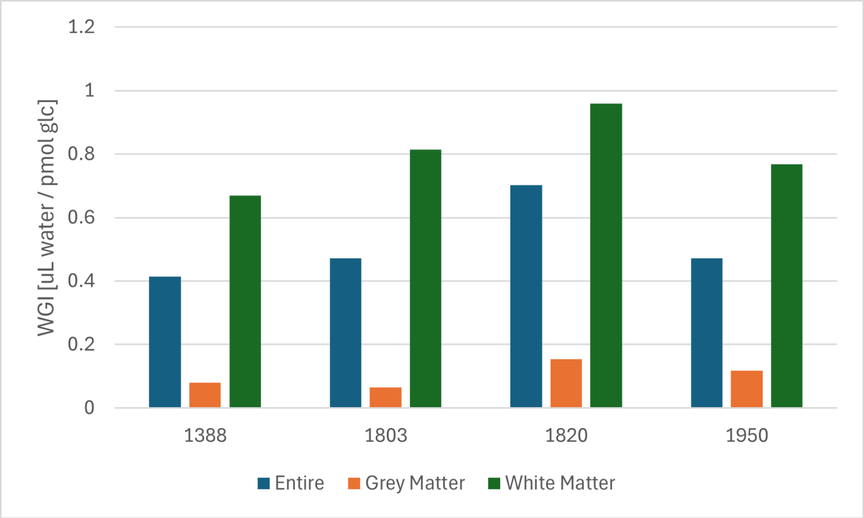

Figure 3.13 Comparison of pROI-Entire's WGI to GM and WM.

Chapter 4

Discussions

4.1 Grey and White Matter - Reference and Scale

The purpose for analysis of GM and WM was twofold: confirm previous measurements, but primarily to develop a sense of scale for the KL divergence. Figure 3.1 establishes that our measurements of GM and WM were not only consistent, but in agreement with previous measurements in Springer et al [1] for cellular volume. Based off these distributions, there should be some level of visual differentiations between GM and WM; this was demonstrated in Figure 3.2. The KL divergence was found for V to be on a 0.1 nat order of magnitude, as seen in Figure 3.3. While direct comparisons of RE are only valid for the same comparison PDF ($p(x)$), a sense of scale can be developed. The visual differentiation between GM and WM can be attributed to a RE on the order of 0.1 nat.

Additionally, Figure 3.1 demonstrates MADI's ability to characterize a tissue's physical properties. Here the V distributions are showing that WM is a tissue comprised of a fairly homogeneous assortment of cells with similar volumes. In contrast, GM is a tissue comprised of cells with great variaition in cellular volume. These tissue properties are supported with in vitro and in vivo measurements [42–44].

4.2 MADI

4.2.1 HBCL Control

Before the KL divergence can be applied to the patient population, it is necessary to show that their comparison PDFs are sufficiently similar / equivalent. That is, in order to compare a RE from one participant to another, say participants i and j, the condition $p_i(x) \simeq p_j(x)$ must be met. In Figure 3.4, ρ and $k_{io}V$ were identified as the best and worst case for the condition being met. By looking at ρ and $k_{io}V$'s PDFs, Figure 3.5, it can be observed that the distributions deviated little from the average, even in the worst case. It was decided that this constitutes the $p_i(x) \simeq p_j(x)$ condition to be met. Additionally, this further establishes a sense of scale for RE that can be compared against; a RE on the order of 0.01 nat is considered to be similar enough to each other.

4.2.2 pROI Selection

As seen in Figure 3.7, there was little differences between the Hollow and Entire pROIs across all parameters despite the Core occasionally being very different, e.g., ρ in pseudoprogression. This can be attributed to the Core only contributing a small fraction of the total pixels. It was decided to move forward with only the Entire pROI for two reasons: simplicity of pROI creation and the similarity of the Hollow and Entire pROIs.

4.2.3 pROI to HBCL

From Figure 3.8, the average REs from comparing the Entire pROIs to the HBCLs is on the order of 0.1 to 1 nat. In comparison to the previous established RE scales, this is 10 to 100 time greater than the HBCL controls and 1 to 10 times greater than the GM and WM controls. This demonstrates that MADI has the ability to differentiate normal tissue, represented by the HBCL, and the pROI.

Additionally, since the tumor and pseudoprogression populations are comparing against the same PDF, we can also use Figure 3.8 to assess progression status. In all parameters the pseudoprogression group had greater RE than the tumor group. While ρ appears to be a stand out parameter, there exists a level of caution due to large variation in the data, i.e. large SE. The smaller error bars indicate that $k_{io}V$ presents the best opportunity for differentiation between tumor and pseudoprogression due to reduced overlap. The KL divergence was performed to assess the differences in the tumor and pseudoprogression groups, as seen in Figure 3.9. It was found that $kioV$ and ρ have the greatest potential for progression status differentiation with RE on the order of 0.1 nat. Within context of ρ having great variation, $k_{io}V$ again becomes the best parameter for progression status differentiation.

While KL divergence allowed for a rigorous analysis of the distributions, it is often desirable to quote a single value for a parameter. For this, a more rudimentary approach was taken by characterizing each parameter by averaging medians for each progression group and tissue ROI, see Figure 3.11 and Table A.1. Through this approach, the differentiation between tumor, pseudoprogression, and HBCL can still be observed in $k_{io}V\rho$. This suggests that, despite not being a rigorous approach, quoting the average of medians may prove to a simpler and viable way to characterize the dataset.

4.3 PET

PET was determined to not be eligible for KL divergence analysis due to great variation in comparison PDFs as seen in Figure 3.6. To analyze the data, ratios of $\mathrm{SUV}_{\mathrm{mean}}$ to the local environment and GM were collected as seen in Figure 3.12. While there was local enhancement of the pROI from its surroundings, the pROI was less intense than GM. For the tumor group this constitutes a false negative for progression status, while the pseudoprogression group was a true negative. Despite this, no trend was observed between progression groups; that is, FDG-PET failed to differentiate tumor and pseudoprogression. This demonstrates FDG-PET's clinical limitation of diminished sensitivity in gliomas. Within this study population, the data suggests that MADI may have greater ability in the assessment of tumor progression than FDG-PET.

4.4 Considerations of Previous Works

This initial MADI study in human brain cancer requires consideration of prior rat research, which primarily compared tumors to contralateral ROIs which were primarily GM. Our approach, conversely, analyzes pROIs against a composite GM and WM HBCL ROI where WM constitutes majority of the tissue type. From Schlegel [2], $k_{io}V$ in rat brain tumor was significantly lower than in contralateral normal tissue (primarily GM). Additionally, from preliminary rat data yet not published, the WGI in tumor was lower than in normal tissue. These finding demonstrate the alteration of cellular metabolism from oxidative phosphorylation, probed by active water cycling, to aerobic glycolysis which is supported by the Warburg effect. In contrast, this behavior was not found in the human data. Figures 3.10 and 3.11 demonstrate the the pROI showed elevated $k_{io}V$ levels in comparison to both GM, WM, and HBCL.

From Figure 3.13, the WGI of pROI-Entire is at minimum 4 times greater than in GM. These results are not consistent with the Warburg effect, though this is not well understood.

4.5 Clinical Implementation

The current protocols in evaluating tumor progression begin by establishing baseline MRI imaging. Pretreatment MRI is used to define the baseline for patients with recurrent glioma. It is recommended that baseline scans be acquired as near as possible to the start of therapy, with a maximum interval of 14 days, particularly for glioblastomas. Followup imaging is performed every two to three months after baseline [25]. That is, progression assessment requires two different time-points. Within MADI's current construction, MADI shows value in assessing tumor progression status with $k_{io}V$ within a single time-point. As patients already undergo MRI imaging, including DWI, the addition of a MADI imaging protocol would add little to patient in-clinic time.

As MADI maps may not demonstrate the greatest visual differentiation, as seen in A.4, their power lies in distribution differentiation. Thus, this works to provide two methods which may be used to track progression status in resected glioma patients. First, requires software development to perform the analysis. A radiologist could create an ROI corresponding to the T1post imaging enhancement and to generate a PDF of $k_{io}V$ to compare to reference normal tissue (GM, WM, or HB), tumor, and pseudoprogression PDFs for tumor progression status evaluation. This would require development of tissue libraries and fitting conditions, such as using KL divergence. Second, a radiologist could create an ROI corresponding to the T1post imaging enhancement and take the median $k_{io}V$ to compare to reference values for evaluation of progression status.

4.6 Limitations

4.6.1 MADI Library

In the current state of MADI, the tissue library is configured for v_i to go as low as 0.5. This limit was set because lower v_is becomes difficult to simulate and were not expected in common applications. When the library matching occurs within MADI, if a tissue that had a true v_i less than 0.5 it would be matched to its closed curve of 0.5 referred to as v_i pegging. Unfortunately resected areas tend to be very 'watery' and diffuse corresponding to a low v_i. Figure 4.1 demonstrates the scope of v_i pegging encountered in these resected areas. At best, 35% of all pixels in a pROI were pegged at v_i. In worst case, 84% of all pROI pixels were pegged. Due to the reproducibility of MADI results, we estimate that despite up to 83% of pixels being pegged, that a v_i of 0.5 is an acceptable approximation for these pixels. We recommend that future MADI improvements should include tissue library curves for v_i less than 0.5.

Additionally within the tissue library, the density of possible matching parameter value tends to decreases as parameter value increase. This can be observed in Figure 3.10 for k_{io} greater than 40 1/s. Here, signal contributions from 47.525, 55.45, 63.375, 71.3, and 95.66 1/s can be resolved, especially for the average HBCL PDF. The only possible k_{io} values within 40 to 100 1/s that can be assigned from the library matching process are these values. As the parameter value density is poorer at higher values, the ability to accurately and precisely characterizes the pixels decreases.

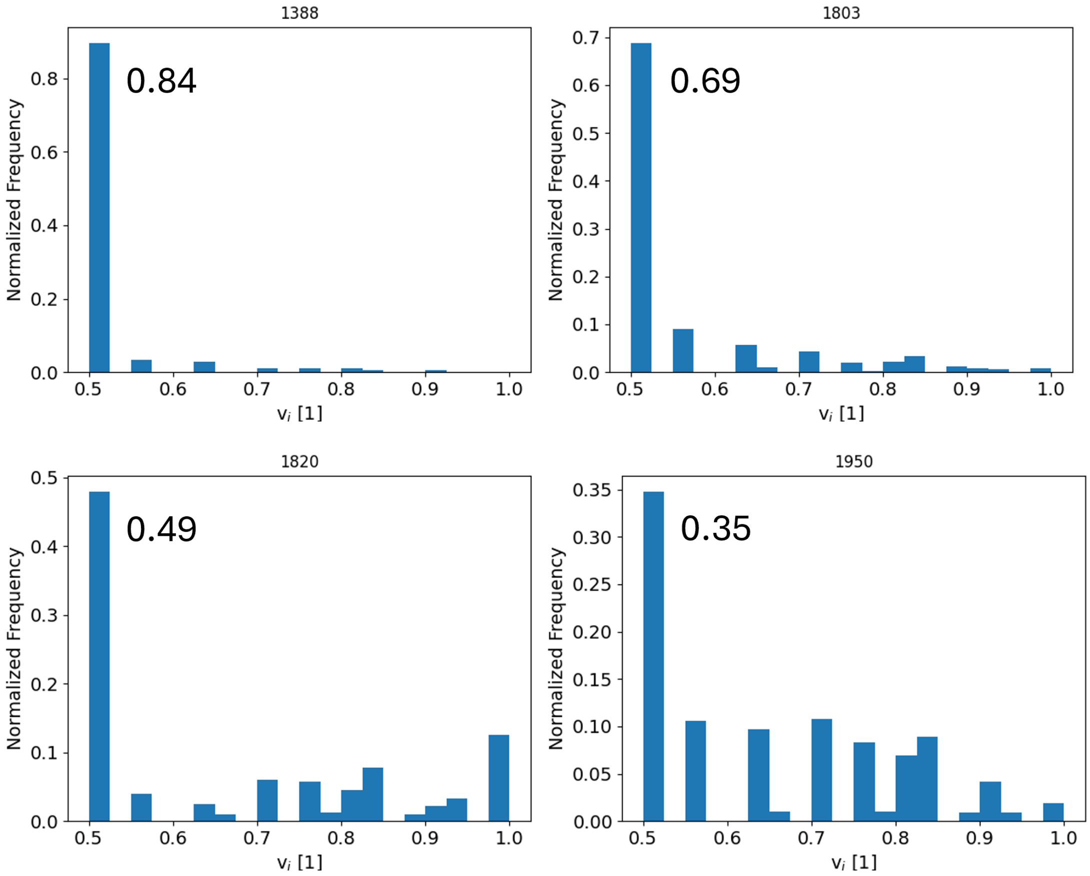

Figure 4.1 Histograms of v_i within the Entire pROI for all participants.

4.6.2 Ill-Fitting Pixels

In looking at the raw ROI data, we had encountered a systematic ill-fitting of pixels, or 'blow-up', as seen in Figures 2.6, A.1, A.2, and A.3. With Vs on the order of 1 pL/cell for GM and WM, this problem skewed the raw data significantly. As Vs up to 180 pL/cell were deemed non-physical, the entirety of the exponential-like curve was deemed an artifact of the MADI computation. Suggestions of methods to remove the artifact data was discussed internally with the MADI-group. We were advised against creating methods that systematically removed the exponential-like function from the datasets as we would need to fully characterize why that exponential-like function exists. This is currently not well understood. A simple 20 pL/cell filter was decided to be adequate for the scope of this Thesis as it prevented extreme skewing and preserved the 'true' data while maintaining the possibility for larger V within the pROI.

An investigation into a previous MADI study was conducted to determine the scope of the ill-fitting pixels problem. Figure A.3 represent the issue present in rat brains from Schlegel [2]. This suggests the problem is an artifact of the MADI approach and is not unique to this study.

As seen in Figure 4.2, there is no correlation between v_i pegging and ill-fitting pixels.

4.6.3 Sample Size

In this study, there were 4 participants total with 2 in each tumor progression group. This is a result of two main factors: project design and institutional protocol change. As outlined in our project design approved by the OHSU IRB, we were to consider imaging exams from the GE Signa PET/MR - 3.0 T. This restricted the population

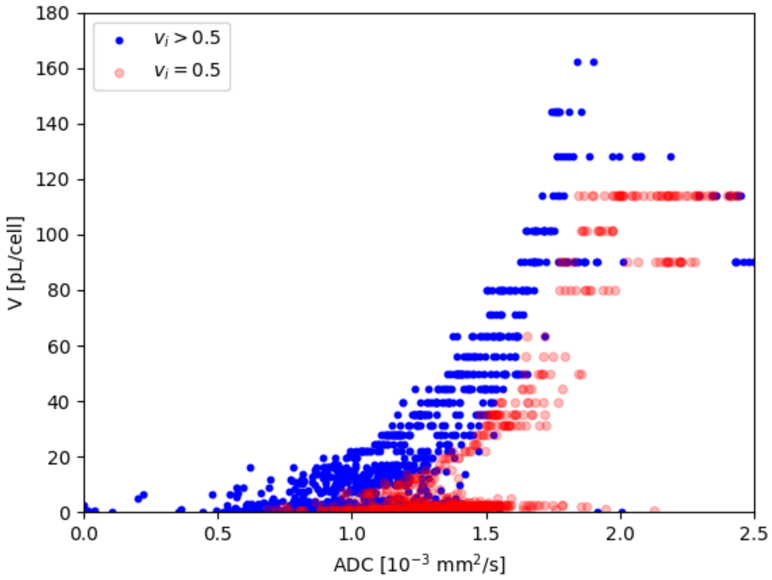

Figure 4.2 Plot of ADC vs. V for pegged (red) and non-pegged (blue) v_i pixels. Data is reflective of participant 1950.

to resected glioma participants only, to which there were few eligible participants. Additionally, OHSU had changed their response assessment of glioma from FDG-PET to amino acid PET, which was outside of the project design. While the sample size was very limited, this work serves as a proof of concept and shows the value of MADI.

4.7 Future Work

Opportunities for future work of MADI are currently in planning. As an extension to this Thesis, a continuation of human glioma investigations with the inclusion of prior resection imaging, histological considerations, and inclusion of amino acid PET is in discussion. Within the field of current MA imaging, preliminary discussions on coupling MADI with ^{13}C MRI imaging would allow for conversion of per tissue quantities to per cell are being explored. In novel applications of MADI, investigations into how changes in metabolic parameters (k_{io}, $k_{kio}V$, $k_{io}V\rho$) within tissue affected areas of Alzheimers, vascular cognitive impairment (VCI), and stroke for mouse studies are in process.

Chapter 5

Conclusions

Representing the first study to employ MADI with human brain cancer, preliminary data was obtained suggesting that MADI has the ability and versatility to probe MA and physical tissue quantities within the human brain and resected gliomas as a non-invasive, contrast-agent-free imaging method. Specifically, MADI demonstrated the ability to differentiate normal tissue, tumor, and pseudoprogression and thus was able to assess tumor progression status. In comparison, FDG-PET, a common MA imager, did not demonstrate this ability. Additionally, preliminary data on the coupling of PET and MADI shows promise on probing the type of metabolism occuing within a cell.

This is an exciting frontier as in underserved and rural populations access to current MA imaging, e.g. PET, may be limited in comparison to DWI-MRI. Beyond tumor progression assessment, by providing both metabolic and cytometric, MADI may provide physicians with additional information to assist in the grading and staging of gliomas.

Bibliography

[1] C. S. Springer Jr *et al.*, "Metabolic activity diffusion imaging (MADI): II. Noninvasive, high-resolution human brain mapping of sodium pump flux and cell metrics," NMR in Biomedicine **36,** e4782 (2023).

[2] J. Schlegel, Ph.D. thesis, Oregon Health & Science University, 2020.

[3] T. Zeuthen, "Molecular water pumps," Reviews of Physiology Biochemistry and Pharmacology: Special Issue on Water Transport Across Biological Membranes pp. 97–151 (2008).

[4] T. Zeuthen, "Water-transporting proteins," Journal of Membrane Biology **234,** 57–73 (2010).

[5] M. Amiry-Moghaddam and O. P. Ottersen, "The molecular basis of water transport in the brain," Nature Reviews Neuroscience **4,** 991–1001 (2003).

[6] R. Bai, C. S. Springer Jr, D. Plenz, and P. J. Basser, "Brain active transmembrane water cycling measured by MR is associated with neuronal activity," Magnetic resonance in medicine **81,** 1280–1295 (2019).

[7] C. S. Springer Jr, "Using 1H2O MR to measure and map sodium pump activity in vivo," Journal of magnetic resonance **291,** 110–126 (2018).

[8] R. Bai, C. S. Springer Jr, D. Plenz, and P. J. Basser, "Fast, Na+/K+ pump driven, steady-state transcytolemmal water exchange in neuronal tissue: A study of rat brain cortical cultures," Magnetic resonance in medicine **79,** 3207–3217 (2018).

[9] A. S. Pivovarov, F. Calahorro, and R. J. Walker, "Na+/K+-pump and neurotransmitter membrane receptors," Invertebrate Neuroscience **19,** 1 (2019).

[10] J. Dunn and M. H. Grider, "Physiology, adenosine triphosphate," (2020).

[11] H. Kurita *et al.*, "Arcuate Na+, K+-ATPase senses systemic energy states and regulates feeding behavior through glucose-inhibited neurons," American Journal of Physiology-Endocrinology and Metabolism **309,** E320–E333 (2015).

[12] J. J. Harris, R. Jolivet, and D. Attwell, "Synaptic energy use and supply," Neuron **75,** 762–777 (2012).

[13] Y. Jia *et al.*, "Transmembrane water-efflux rate measured by magnetic resonance imaging as a biomarker of the expression of aquaporin-4 in gliomas," Nature Biomedical Engineering **7,** 236–252 (2023).

[14] M. R. Ruggiero, S. Baroni, S. Pezzana, G. Ferrante, S. Geninatti Crich, and S. Aime, "Evidence for the role of intracellular water lifetime as a tumour biomarker obtained by in vivo field-cycling relaxometry," Angewandte Chemie **130,** 7590–7594 (2018).

[15] C. S. Springer Jr, E. M. Baker, X. Li, B. Moloney, G. J. Wilson, M. M. Pike, T. M. Barbara, W. D. Rooney, and J. H. Maki, "Metabolic activity diffusion imaging (MADI): I. Metabolic, cytometric modeling and simulations," NMR in Biomedicine **36,** e4781 (2023).

[16] H. Ohgaki and P. Kleihues, “Population-based studies on incidence, survival rates, and genetic alterations in astrocytic and oligodendroglial gliomas,” Journal of Neuropathology & Experimental Neurology **64,** 479–489 (2005).

[17] J. D. Olson, E. Riedel, and L. M. DeAngelis, “Long-term outcome of low-grade oligodendroglioma and mixed glioma,” Neurology **54,** 1442–1448 (2000).

[18] E. A. Maher, F. B. Furnari, R. M. Bachoo, D. H. Rowitch, D. N. Louis, W. K. Cavenee, and R. A. DePinho, “Malignant glioma: genetics and biology of a grave matter,” Genes & development **15,** 1311–1333 (2001).

[19] A. F. Tamimi and M. Juweid, “Epidemiology and outcome of glioblastoma,” Exon Publications pp. 143–153 (2017).

[20] P. Vaupel, H. Schmidberger, and A. Mayer, “The Warburg effect: essential part of metabolic reprogramming and central contributor to cancer progression,” International journal of radiation biology **95,** 912–919 (2019).

[21] R. Moreno-Sánchez, D. X. Robledo-Cadena, S. C. Pacheco-Velázquez, J. L. V. Navarro, J. A. Padilla-Flores, and S. Rodríguez-Enríquez, “Estimation of energy pathway fluxes in cancer cells-Beyond the Warburg effect,” Archives of Biochemistry and Biophysics **739,** 109559 (2023).

[22] M. G. Vander Heiden, L. C. Cantley, and C. B. Thompson, “Understanding the Warburg effect: the metabolic requirements of cell proliferation,” science **324,** 1029–1033 (2009).

[23] M. V. Liberti and J. W. Locasale, “The Warburg effect: how does it benefit cancer cells?,” Trends in biochemical sciences **41,** 211–218 (2016).

[24] P. Y. Wen *et al.*, “RANO 2.0: update to the response assessment in neuro-oncology criteria for high-and low-grade gliomas in adults,” Journal of Clinical Oncology **41,** 5187–5199 (2023).

[25] N. L. Albert *et al.*, “PET-based response assessment criteria for diffuse gliomas (PET RANO 1.0): a report of the RANO group,” The Lancet Oncology **25,** e29–e41 (2024).

[26] N. Quartuccio *et al.*, “The additional value of 18F-FDG PET and MRI in patients with glioma: a review of the literature from 2015 to 2020,” Diagnostics **10,** 357 (2020).

[27] A. Verger and K.-J. Langen, “PET Imaging in glioblastoma: Use in clinical practice,” Exon Publications pp. 155–174 (2017).

[28] J. Bolcaen, M. Acou, B. Descamps, K. Kersemans, K. Deblaere, C. Vanhove, and I. Goethals, “PET for therapy response assessment in glioblastoma,” Exon Publications pp. 175–195 (2017).

[29] D. W. McRobbie, E. A. Moore, M. J. Graves, and M. R. Prince, *MRI from Picture to Proton* (Cambridge university press, 2017).

[30] J. T. Bushberg and J. M. Boone, *The essential physics of medical imaging* (Lippincott Williams & Wilkins, 2011).

[31] S. R. Cherry, J. A. Sorenson, and M. E. Phelps, *Physics in nuclear medicine* (Saunders, 2013).

[32] N. Galldiks, M. Kocher, and K.-J. Langen, “Pseudoprogression after glioma therapy: an update,” Expert review of neurotherapeutics **17,** 1109–1115 (2017).

[33] G. Santo *et al.*, "The utility of conventional amino acid PET radiotracers in the evaluation of glioma recurrence also in comparison with MRI," Diagnostics **12,** 844 (2022).

[34] A. Zikou, C. Sioka, G. A. Alexiou, A. Fotopoulos, S. Voulgaris, and M. I. Argyropoulou, "Radiation necrosis, pseudoprogression, pseudoresponse, and tumor recurrence: imaging challenges for the evaluation of treated gliomas," Contrast media & molecular imaging **2018,** 6828396 (2018).

[35] K. Herholz, "Brain tumors: an update on clinical PET research in gliomas," In *Seminars in nuclear medicine*, **47,** 5–17 (2017).

[36] S. P. Devan *et al.*, "Selective cell size MRI differentiates brain tumors from radiation necrosis," Cancer research **82,** 3603–3613 (2022).

[37] X. Jiang, H. Li, J. Xie, P. Zhao, J. C. Gore, and J. Xu, "Quantification of cell size using temporal diffusion spectroscopy," Magnetic resonance in medicine **75,** 1076–1085 (2016).

[38] E. Panagiotaki, S. Walker-Samuel, B. Siow, S. P. Johnson, V. Rajkumar, R. B. Pedley, M. F. Lythgoe, and D. C. Alexander, "Noninvasive quantification of solid tumor microstructure using VERDICT MRI," Cancer research **74,** 1902–1912 (2014).

[39] O. Reynaud, K. V. Winters, D. M. Hoang, Y. Z. Wadghiri, D. S. Novikov, and S. G. Kim, "Pulsed and oscillating gradient MRI for assessment of cell size and extracellular space (POMACE) in mouse gliomas," NMR in biomedicine **29,** 1350–1363 (2016).

[40] D. W. Scott, *Multivariate density estimation: theory, practice, and visualization* (John Wiley & Sons, 2015).

[41] C. R. Bartman *et al.*, "Slow TCA flux and ATP production in primary solid tumours but not metastases," Nature **614,** 349–357 (2023).

[42] T. P. Naidich, E. A. Nimchinsky, and P. Pasik, "CerebralCerebral CortexCortex," Imaging of the Brain E-Book: Expert Radiology Series p. 154 (2012).

[43] Y. Assaf and Y. Cohen, "Inferring microstructural information of white matter from diffusion MRI," in *Diffusion MRI* (Elsevier, 2014), pp. 185–208.

[44] J. M. Edgar and I. R. Griffiths, "White matter structure: a microscopist's view," in *Diffusion Mri* (Elsevier, 2014), pp. 127–153.

Appendix A

Appendix

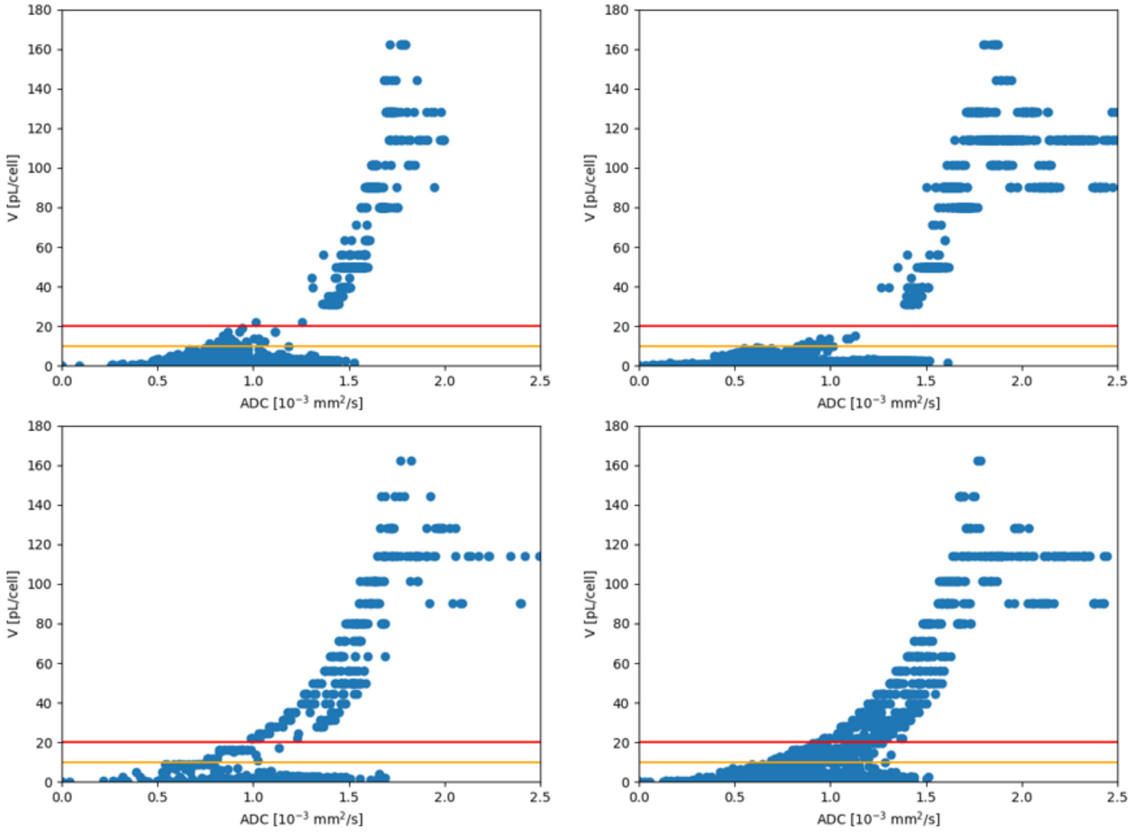

Figure A.1 Plots of ADC vs V for all participants. Orange and red lines are 10 and 20 pL/cell, respective. Plots correspond to participants 1388 (top left), 1803 (top right), 1820 (bottom left), and 1950 (bottom right).

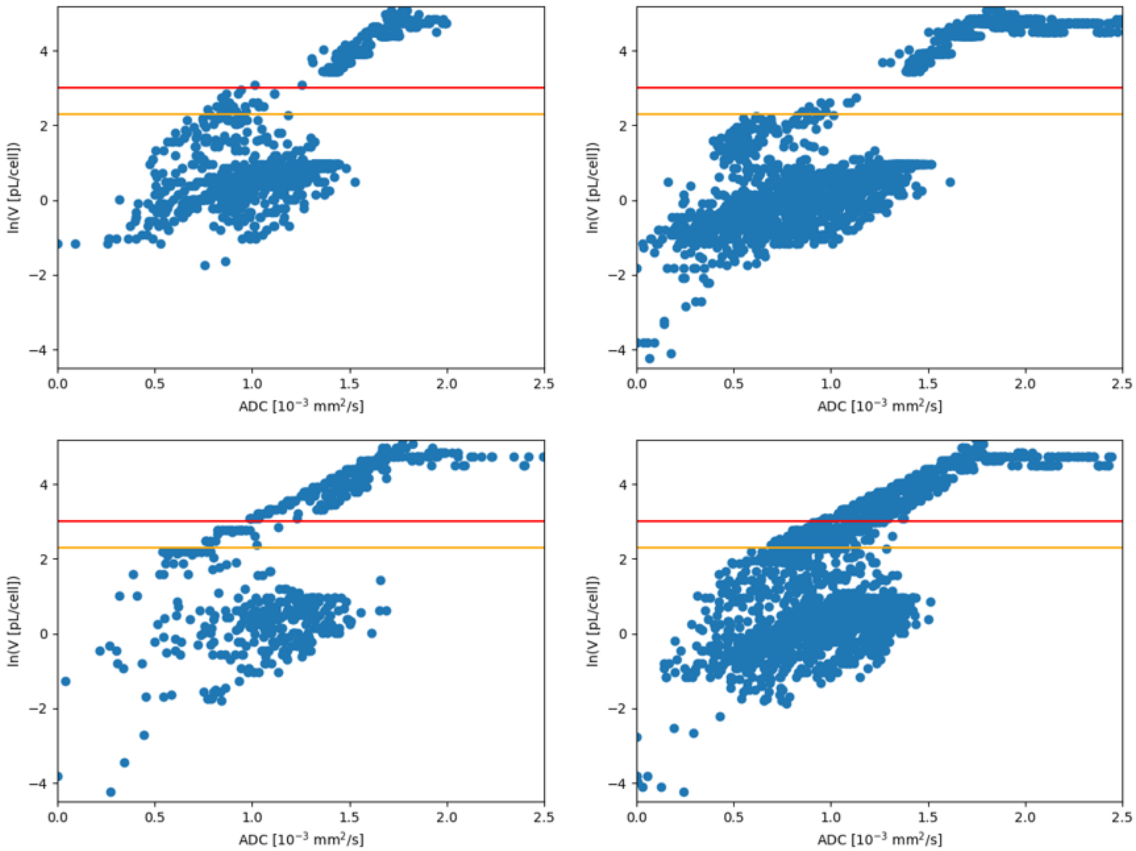

Figure A.2 Plots of ADC vs $\ln(V)$ for all participants. Orange and red lines are 10 and 20 pL/cell, respective. Plots correspond to participants 1388 (top left), 1803 (top right), 1820 (bottom left), and 1950 (bottom right).

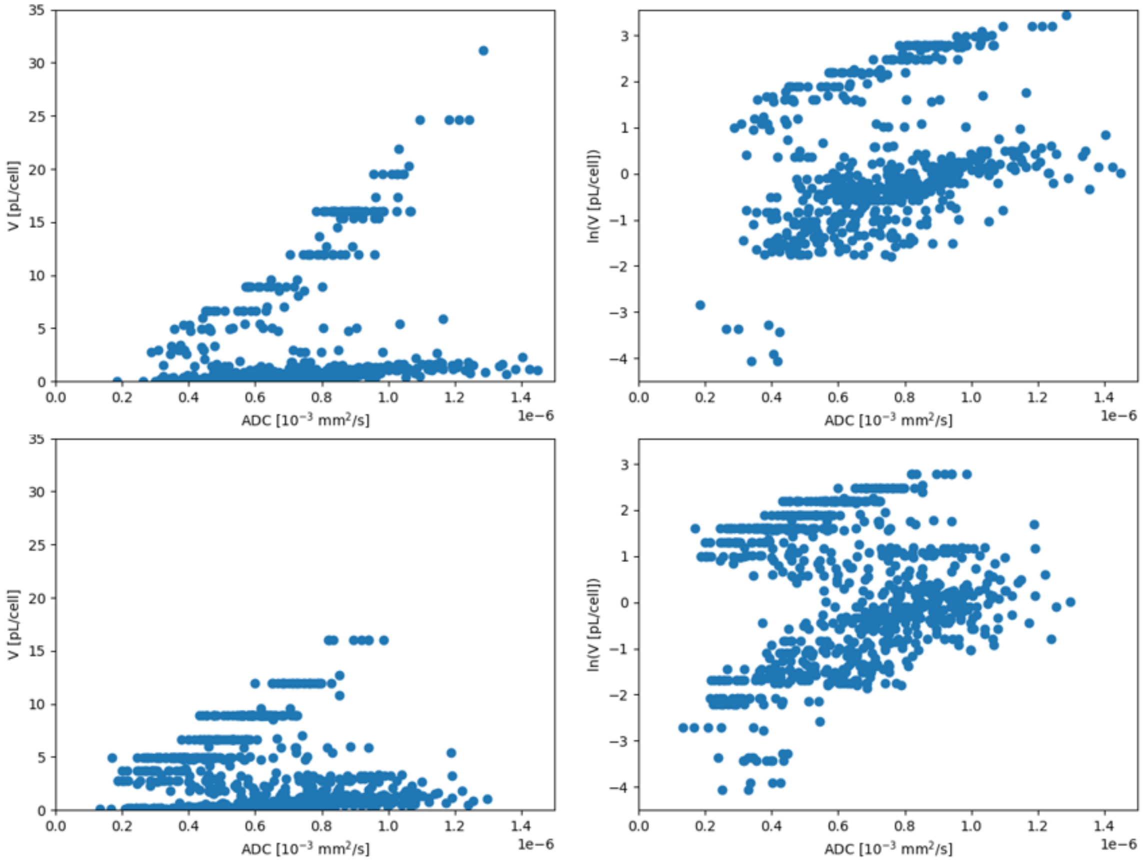

Figure A.3 Plots of ADC vs V in both linear and logarithmic scales for mice BIP-1 and BIP-4 used in Schlegel [2]. Orange and red lines are 10 and 20 pL/cell, respective.

$\langle\text{median}\rangle \pm \text{SE}$	k_{io} [1/s]	$k_{io}V$ [pL/s/cell]	$k_{io}V\rho$ [10^5 pL/s/uL]	ρ [10^5 cells/uL]	V [pL/cell]	v_i [1]
Tumor	33.73 ± 0	36.33 ± 4.24	179.2 ± 10.5	4.210 ± 0.124	1.274 ± 0.186	0.566 ± 0.066
Pseudoprogression	36.67 ± 2.93	54.21 ± 1.12	183.3 ± 14.7	3.065 ± 0.359	1.698 ± 0.150	0.531 ± 0.031
HBCL	22.00 ± 0	19.14 ± 0.49	121.0 ± 4.36	4.897 ± 0.263	1.081 ± 0.0426	0.712 ± 0
GM	16.42 ± 4.26	24.10 ± 0.28	100.1 ± 15.9	1.909 ± 0.299	3.480 ± 0.678	0.811 ± 0.010
WM	23.47 ± 1.47	16.53 ± 1.56	148.5 ± 9.28	8.597 ± 0.639	0.8307 ± 0.0647	0.698 ± 0.014

Table A.1 Collection of average medians for each MADI parameter for tumor and pseudoprogression groups and in different locations in the brain.

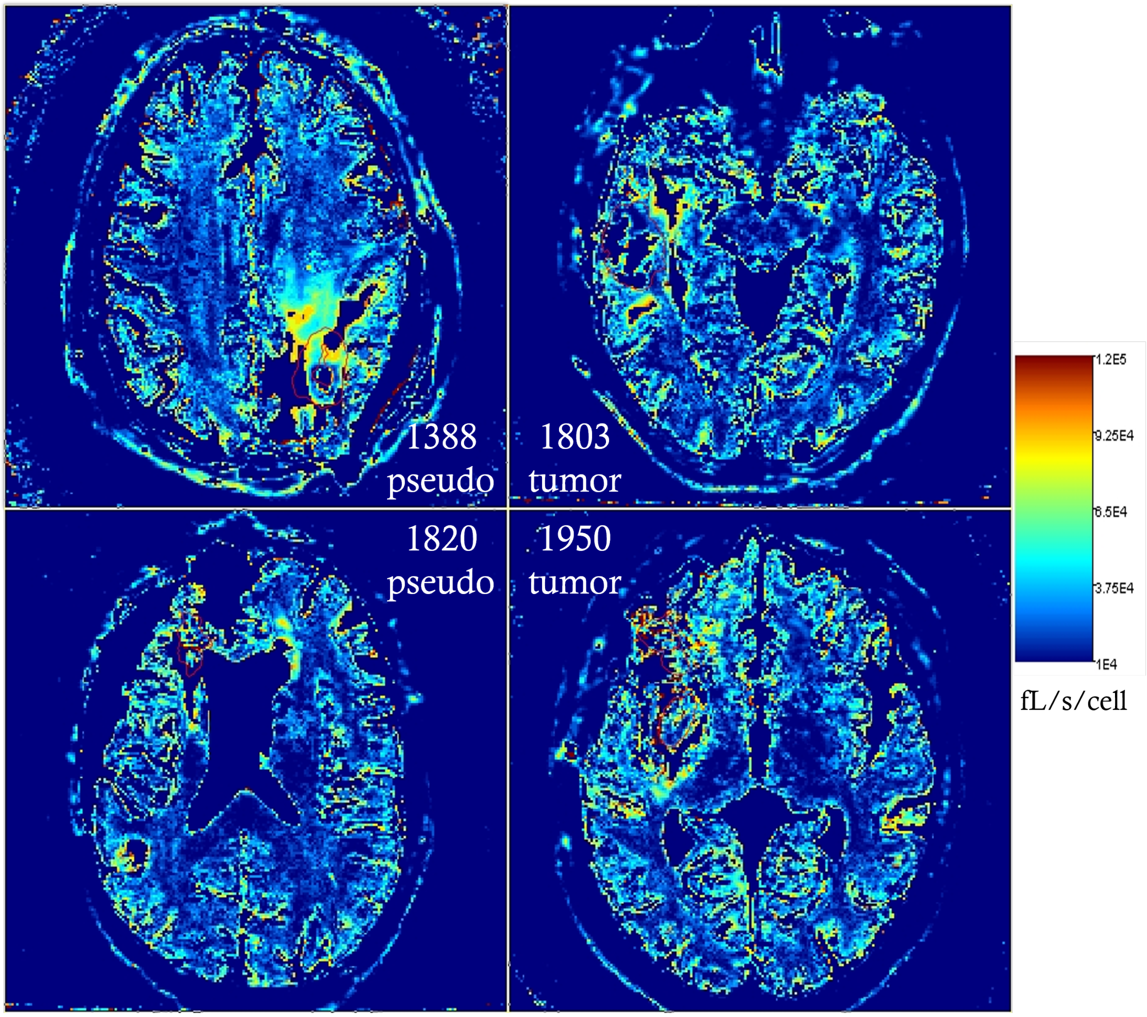

Figure A.4 Maps of $k_{io}V$ for all participants with pROI-Hollow.